Journal of Manufacturing Processes 82 (2022) 829–847

Contents lists available at ScienceDirect

Journal of Manufacturing Processes

journal homepage: www.elsevier.com/locate/manpro

Effect of preheating and preplaced filler wire on microstructure and toughness in laser-arc hybrid welding of thick steel

Ivan Bunaziv [a,*], Geir Langelandsvik [a], Xiaobo Ren [b], Ida Westermann [c], Gisle Rørvik [d], Cato Dørum [e], Morten Høgseth Danielsen [a], Magnus Eriksson [a]

[a] Materials and Nanotechnology, SINTEF Industry, P.O. Box 4760 Torgarden, NO-7465 Trondheim, Norway
[b] Metal Production and Processing, SINTEF Industry, NO-0314 Oslo, Norway
[c] Department of Materials Science and Engineering, Norwegian University of Science and Technology (NTNU), Alfred Getz vei 2, NO-7491 Trondheim, Norway
[d] Equinor ASA, Research Centre – Rotvoll, Arkitekt Ebbells veg 2, NO-7053 Ranheim, Norway
[e] Norwegian Public Roads Administration, Bridge Section, NO-2317 Hamar, Norway

ARTICLE INFO

Keywords:
Laser-arc hybrid welding
High strength steel
Preheating
Non-metallic inclusions
Acicular ferrite
Microstructure
Impact toughness
Solidification cracking

ABSTRACT

Acicular ferrite (AF) is the most important microstructural constituent to achieve high toughness at low temperatures in weld metal of steels. This is due to the relatively small grain size and large misorientation angles. AF is known to form at non-metallic inclusions (NMIs), but under high cooling rates, as in deep and narrow laser-arc hybrid welding (LAHW), this phenomenon is scarcely studied. In deep and narrow LAHW, insufficient transportation of filler wire to the root results in low amount of NMIs, thus bainite-martensite mainly forms due to fast cooling. In this work, a 45 mm thick high strength low alloy steel was welded by double-sided LAHW using different groove preparations. The effect of different cooling times on the microstructure in the weld metal and the heat-affected zone was studied. A low fraction of AF and high hardness were achieved in the root of weld metal when using standard LAHW. This was related to a rapid cooling time ($\Delta t_{8/5} < 1.0$ s) and a low population of NMIs due to lack of filler wire. Micro X-ray computed tomography revealed centerline solidification cracks and porosity. Two external methods were conducted to assist the formation of AF and to reduce hardness, base plate preheating and preplaced metal-cored filler wire into the weld groove prior to welding. Preheating reduced hardness and increased the AF fraction due to increased cooling time. In addition, preheating showed to mitigate porosity. Preplaced filler wire provided an enhanced population of NMIs in the root thus significantly increased the fraction of AF. It was found that the diameter and chemical composition of NMIs has a strong correlation with the cooling time $\Delta t_{8/5}$. High impact toughness (> 35 J) was achieved at -50 °C by combining preheating and preplaced filler wire, and up to 45 % fraction content of AF was reached. However, many NMIs were still inactive due to a small diameter (< 200 nm) and unfavorable chemical composition related to the high cooling rate. The external methods had no influence on the occurrence of weld centerline cracks in the root, which will require further attention to secure mechanical properties and integrity.

1. Introduction

The most widely used technique for joining of thick steel components is the multi-pass fusion welding, which is also the main process for many heavy steel fabrication industries, e.g., offshore installations and shipbuilding. The term thick, or heavy steel, is ambiguous since it depends

Abbreviations: AF, acicular ferrite; B, bainite; BM, base metal; CGHAZ, coarse-grained heat-affected zone; CT, computed tomography; CVN, Charpy V-notch; EDS, energy dispersive spectroscopy; FGHAZ, fine-grained heat-affected zone; FL, fusion line; GB, granular bainite; GBF, grain boundary ferrite; GMAW, gas metal arc welding; HAZ, heat-affected zone; HSLA, high-strength low alloy; HV, Vickers hardness; ICCGHAZ, intercritically reheated coarse-grained heat-affected zone; ICHAZ, intercritical heat-affected zone; IWF, intragranular Widmanstätten ferrite; J, joule; LAHW, laser-arc hybrid welding; LB, lower bainite; LBW, laser beam welding; LM, lath martensite; M-A, martensite-austenite; NMIs, non-metallic inclusions; P_A, arc power output; P_L, laser beam power output; PAG, prior austenite grain; Q_A, heat input of arc; Q_H, heat input of hybrid welding; Q_L, heat input of laser beam; SEM, scanning electron microscopy; UB, upper bainite; UCGHAZ, unaltered coarse-grained heat-affected zone; WF, Widmanstätten ferrite; WM, weld metal.

* Corresponding author.
E-mail address: ivan.bunaziv@sintef.no (I. Bunaziv).

https://doi.org/10.1016/j.jmapro.2022.08.026
Received 1 June 2022; Received in revised form 15 August 2022; Accepted 18 August 2022
Available online 2 September 2022
1526-6125/© 2022 The Author(s). Published by Elsevier Ltd on behalf of The Society of Manufacturing Engineers. This is an open access article under the CC BY license (http://creativecommons.org/licenses/by/4.0/).

on the industry and application. Therefore, in this work the term indicates a thickness of welded plates within the range of 15—50 mm. Laser beam welding (LBW) and laser-arc hybrid welding (LAHW) have been used for decades in highly automated industries such as automotive, aerospace, and shipbuilding primarily for joining thin sheets. Solid-state, high-power ytterbium fiber and disk lasers became available for industrial use in 2004. Disk lasers are limited to 24 kW power output. Nowadays, they are rapidly substituting CO_2 (maximum of 20 kW) and Nd:YAG (maximum of 8 kW) lasers due to higher energy efficiency, flexibility, and low maintenance costs. This opened many possibilities to weld thick steel in only one or few passes. A high-power multi-mode laser beam can be finely focused to a 150—800 μm spot diameter. When the power density reaches a threshold of $>10^6$ W/cm^2, the intensive evaporation causes the formation of a keyhole (or vapor filled capillary) sustained by a recoil pressure through the internal multiple reflection mechanism, which then provide high penetration depths [1]. As a result, the productivity can be more than twenty times higher than conventional arc welding.

One of the first articles regarding the use of high-power fiber lasers for low carbon steels was published in 2007 by Quintino et al. [2], where autogenous LBW with 8 kW Yb:fiber laser (0.6 mm focus spot diameter) at 1 m/min welding speed was able to achieve a 6 mm deep weld. Sokolov et al. [3] reported in 2011 full penetration of a 25 mm thick steel using 30 kW Yb:fiber laser (0.42 mm focus spot diameter) by single-pass welding technique. According to Shcherbakov et al. [4], IPG Photonics introduced the first continuous-wave 100 kW Yb:fiber laser prototype in 2013. Then, in 2018 Kawahito et al. [5] demonstrated ultra-deep welding of stainless steel achieving 70—75 mm penetration depth in single-pass at 0.3 m/min welding speed with 1.0 mm focus spot diameter. It was shown by Katayama et al. [6] that welding in vacuum may provide extraordinary improvements in penetration depths due to suppression of the weld plume. Reisgen et al. [7] demonstrated full penetration of 50 mm thick steel using only 16 kW fiber laser with single-pass at 10 Pa ambient pressure. However, welding in vacuum requires special and expensive equipment, which is less likely to be viable on an industrial scale today. Moreover, the mechanical properties of such welds have not been reported.

It has been shown that deep welds produce high hardness in the fusion zone, commonly referred to as the weld metal (WM). In some examples of autogenous LBW of low carbon X100 steel (0.025 wt% C), hardness in the root area has reached 390 HV due to extensive martensite formation at the weld depth of 6.2 mm, and thereby representing a 50 % hardness increase compared to the base metal [8]. An increased heat input from the laser beam (from 0.16 to 0.96 kJ/mm), only slightly reduced the hardness in the root with a marginal increase of penetration depths. In autogenous LBW of 20 mm thick steel with higher carbon content (0.20 wt%), hardness in the fusion zone even exceeded 500 HV, which is an increase by 156 % from the base metal [3]. Therefore, the narrow weld geometry and higher carbon content affecting hardenability are important factors related to hardness increase in the root area.

The increased hardness and high cooling rates involved in deep LBW/LAHW frequently provides cracking and porosity issues. Cracking is a common problem that mainly occurs at the weld centerline near the root area, due to the stress field during solidification [9], and is commonly referred to as solidification or hot cracking [10]. Porosity mainly forms due to unstable keyhole conditions providing poor degassing in combination with fast solidification in deep welds [11].

Autogenous LBW can be used with an external filler wire fed into the weld pool, but it can be challenging to apply due to a small beam diameter. The use of LAHW is more feasible due to the inherent ability to add a filler metal for improvement of mechanical properties through microstructural refinement. The most attractive arc process is gas metal arc welding (GMAW) due to a high filler metal deposition. Filler wire provides extra metal for a slight weld reinforcement and reduce the undercut that can be formed at higher welding speeds. Moreover, an additional heat input from the arc may reduce hardness by increasing the cooling time, as demonstrated by Üstündağ et al. [12]. One of the main issues in thick metal welding is poor filler wire distribution into the root area in narrow and deep welds. Bunaziv et al. [13] showed that, in some cases, a low volume fraction of filler wire is transported towards the root area during welding, hence the resulting microstructure was predominantly consisting of lath martensite and bainite. Another main challenge of LAHW is the vast number of parameters in addition to many interacting phenomena [14,15].

Acicular ferrite (AF) forms during solid-state transformation in the temperature range from 800 °C to 500 °C upon cooling (denoted as $\Delta t_{8/5}$) and has been studied for many decades mainly for conventional arc welding or steel production because of the good combination of strength and toughness [16]. Therefore, it is also a highly desirable microstructure for low temperature applications, due to a small, highly misoriented or interlocked grain structure [17–19]. According to Akselsen and Grong [20], a 25 % volume fraction of AF is needed to achieve >35 J toughness at low temperature (−50 °C) for carbon steels with 600 MPa tensile strength. Furthermore, >70 % volume fraction of AF may provide >70 J at −50 °C for a similar steel. AF nucleates at non-metallic inclusions (NMIs) and its nucleation mechanism is intricate due to many interacting phenomena. Moreover, there are many contradicting factors due to the interdependence of these phenomena. For further study, Loder et al. [21] provide an extensive overview on the AF nucleation. In deep welds, the root area mainly consists of the remelted base metal (BM) due to high dilution. As a result, the nucleation of AF there is hampered since the weld metal contains too low amounts of NMIs.

The study of filler wire distribution in deep welds is of great interest and is challenging since its concentration in the WM at the root is difficult to estimate. A fast and easy solution to study the depth of filler wire distribution is to apply a highly alloyed filler wire, such as stainless steel filler wire in LAHW of carbon steel base metal. This provides a visible discoloration from the etching response [22,23]. Such technique has also been demonstrated by other studies [24–26]. However, welded specimens with such wires are not relevant for the assessment of mechanical properties. Moreover, physical phenomena may deviate from the one found in conventional carbon steel base metals to a carbon steel filler wire combination due to different thermo-physical properties. Carbon steel filler wires have a similar chemical composition as the BM. Therefore, the discoloration can be ambiguous. As an alternative, the filler wire distribution can be assessed based on the density of NMIs. This method is more time-consuming, but is reliable as shown by Bunaziv et al. [27]. It was identified that a small portion of the filler wire is usually present in the root. Further optimization of parameters may increase the delivery of filler wire towards the weld root, but it is still strongly limited. The use of preplaced filler metal into a groove prior to welding was demonstrated by Wahba et al. [28], where LAHW of 25 mm thick steel was welded by a double-sided technique. However, the effect of preplaced filler wire on AF nucleation and resulting mechanical properties were not assessed.

Preheating of specimens prior to welding may reduce the hardness and increase toughness. It introduces additional costs but may substitute the need of expensive post-weld heat treatments. In the case of high strength steels, preheating frequently provides improved mechanical properties as indicated by Li et al. [29]. According to Turichin et al. [30], the hardness was reduced from 343 HV to 300 HV for a 23.7 mm thick X80 carbon steel when 180 °C preheating temperature was applied prior to welding. Preheating increased the cooling time ($\Delta t_{8/5}$) by a factor of three (from 0.51 s to 1.67 s) thus the impact toughness was improved due to martensite suppression.

Within the research area of deep penetration LAHW of thick steels, there are many issues to be solved. Most of these issues derives from high depth-to-width ratio of weld geometry and requires to be considered at the same time. Usually, researchers concentrate on a specific issue. Henceforth, intensive studies are required to implement LAHW for industrial use and comply with standards. A typical commercial high-

power laser system offers maximum laser power output in the range of 10—15 kW. The maximum penetration depth is then usually limited to 20—25 mm, depending on setup and process parameters. Therefore, a 45 mm thick steel was chosen in this study to understand the process limitations using double-sided welding technique. Such plate thicknesses have high interest in the offshore industry to minimize production costs. According to the authors' knowledge, completely defect-free welds with high mechanical properties under standard welding conditions (without vacuum) for 40—45 mm thick steel plates have not yet been revealed. The challenge intensifies when a high strength low alloy (HSLA) steel is used, which is more prone to cracking and hardening. Moreover, the heat input should be also restricted due to softening in heat-affected zone (HAZ). In this work, a 520 MPa yield strength HSLA steel was chosen which is similar to the widely used X80 grade pipeline steel. The main objective of this work is to demonstrate the viability of LAHW for thick HSLA steel combined with a comprehensive study of weld quality in terms of microstructure and internal imperfections, and its correlation with the toughness at low temperatures.

The effect of preheating on hardness is straightforwardly simple but its effect on the microstructure and toughness is scarcely studied in the case of thick plates. Furthermore, its effect on the AF nucleation, porosity, and cracking has not been explicitly revealed. Commercial filler wires are mainly developed for conventional arc welding where the cooling time $\Delta t_{8/5}$ is prolonged and large prior austenite grains (PAGs) are formed providing a high AF volume fraction [31]. In deep and narrow welds, the cooling time is substantially shorter along with small PAGs in the root area that significantly suppresses the nucleation of AF. Moreover, a comprehensive behavior of NMIs at fast cooling rates ($\Delta t_{8/5} < 1.0$ s) is poorly understood. Some studies indicating that high cooling rates hinder the nucleation and growth of AF platelets [32]. This work explicitly reveals the characterization of NMIs and the microstructure at fast cooling rates. Since it is challenging to control the amount of filler wire mixed into the root area, preplaced filler wire was used prior to welding. Later, both preheating and preplaced filler wire were used simultaneously that provided extended data on the behavior of NMIs. The study of crack formation during welding is a significant challenge, especially in thick steels since high X-ray penetrability is required. Micro X-ray computed tomography (CT) was used to reveal internal imperfections explicitly in a three-dimensional space.

As a first attempt, I-groove beveling preparation was used since it is the simplest option when using double-sided welding technique. These initial tests resulted in lack of penetration and high hardness in the root area. Preheating of the BM to 240 °C prior to welding further reduced hardness and improved the microstructure but provided softening in the upper part of the welds. CT revealed high porosity content and solidification cracking at the weld centerline. In the continuation, Y-groove beveling was used which provided full penetration. AF nucleation under the ultra-fast cooling effect was elucidated and the characteristics of NMIs were explicitly analyzed at different penetration depths. The two external methods were used prior to welding to study their effect on the microstructure. Preheating to 170 °C reduced porosity but had a minor effect on the cracking mitigation. However, by increasing the cooling time $\Delta t_{8/5}$ for AF nucleation the microstructure was noticeable improved. The experiments with preplaced filler wire into the groove increased the amount of NMIs in the weld metal, thus increasing the AF content. The combination of both external methods provided 45—50 vol % of AF and a corresponding high impact toughness (> 40 J) at −50 °C was achieved. The fractographic surface characterization of the Charpy V-notch samples by scanning electron microscopy revealed the transition from cleavage to fibrous fracture mode with an increase of AF vol%. The effect of cooling time $\Delta t_{8/5}$ was correlated with microstructure, hardness, NMIs, AF formation, and impact toughness. Despite that favorable microstructures were achieved, the use of standard LAHW, even with preheating and preplaced filler wire, was not capable to provide fully qualified welds, mainly due to internal imperfections. Therefore, solidification cracking at weld centerline is the one of main issues in deep welds, which requires further investigations.

2. Methodology

2.1. Equipment and experimental procedure

A continuous wave, 16 kW maximum power output ytterbium fiber laser (IPG Photonics YLS-16000-S2 type model) was used with the following parameters: 300 μm fiber core diameter, beam parameter product of 12 mm•mrad, and 1070 nm wavelength. The laser beam had an approximate Gaussian heat distribution with the following optical parameters: 300 mm focal length, focused spot diameter 512 μm (as measured), and Rayleigh length of 5.6 mm (as measured). The laser beam was inclined by 8° from the normal towards the welding surface to eliminate back reflections. The GMAW torch had a 55° inclination angle. The welds were made with an articulated robot manipulator and the setup is shown in Fig. 1a. Constant welding parameters within this work were: 15 ± 1 mm filler wire stick-out, 82 % Ar-18 % CO_2 shielding gas at 25 L/min flow rate, and the laser-arc interdistance (D_{LA}) was 4—5 mm. The spray arc mode was used in all experiments. The focal point position was located −4 mm down into the steel plates for the I-groove beveling, and −7 mm down for the Y-groove. Ultra-high-power laser beam welding forms a dense plasma plume above the keyhole and in this work up to 15 cm in height. Therefore, a twin air-knife system was used to remove the plasma plume and eliminate spatter impingement on a protection glass of the optics. The first air-knife (compressed air up to 8 bar) was located just above the arc torch and the secondary air-knife (compressed air up to 5 bar) was located at 10 cm above the plate surface.

The base metal used was a 45 mm thick high strength low alloy (HSLA) steel. The plates were cut to 500 × 120 × 45 mm^3 specimen size. Run-in and run-out plates were welded to the steel plates to secure constant air gap. A simple I-groove geometry was initially used (see Fig. 1b) with finely milled edges providing low roughness ($R_a = 1.6$ μm). The top surface was degreased with acetone to avoid contamination, and oxides were removed mechanically. The Y-groove beveling was used with a similar milling quality (see Fig. 1c). A special groove preparation was used for the preplaced filler wire to hinder their movement during melting (see Fig. 1d). The steps (or noses, with a 0.4 mm width) were introduced in the middle of the plate to prevent melt drop-out. The preplaced filler wire was cut into pieces of 80—90 mm in length, stacked on each other in three layers, and squeezed to 0.8 mm to fit the air gap.

A low carbon steel metal-cored filler wire (designated T 50 6 1Ni M M21 1 H5 based on EN ISO 17632-A) was used with 1.2 mm in diameter and low level of diffusible hydrogen (< 3 mL per 100 g in weld metal). The chemical composition and mechanical properties of the BM and the filler wire are outlined in Tables 1 and 2, respectively.

A summary of welding parameters is indicated in Table 3. A welding speed of 0.8 m/min was identified as minimum velocity at 15 kW power due to experimental limitations. It was found that at low welding speeds and high-power emission a large weld plume was generated which frequently damaged the protection glass of the optics. Note that the weld without preplaced filler wire nor preheating is called the standard LAHW.

The total line energy input for LAHW (Q_H, kJ/mm) is calculated as a sum of the laser beam energy input (Q_L, kJ/mm) and the arc energy input (Q_A, kJ/mm):

$$Q_H = Q_L + Q_A = \frac{P_L \cdot \eta_L}{1000 \cdot v_t} + \frac{P_A \cdot \eta_A}{1000 \cdot v_t} \quad (1)$$

Where P_L is the laser power (in W), P_A is the arc power (in W), v_t is the welding speed (mm/s), η_A is the arc efficiency factor (0.8 for GMAW), and η_L is the laser beam efficiency (assumed to be 0.7).

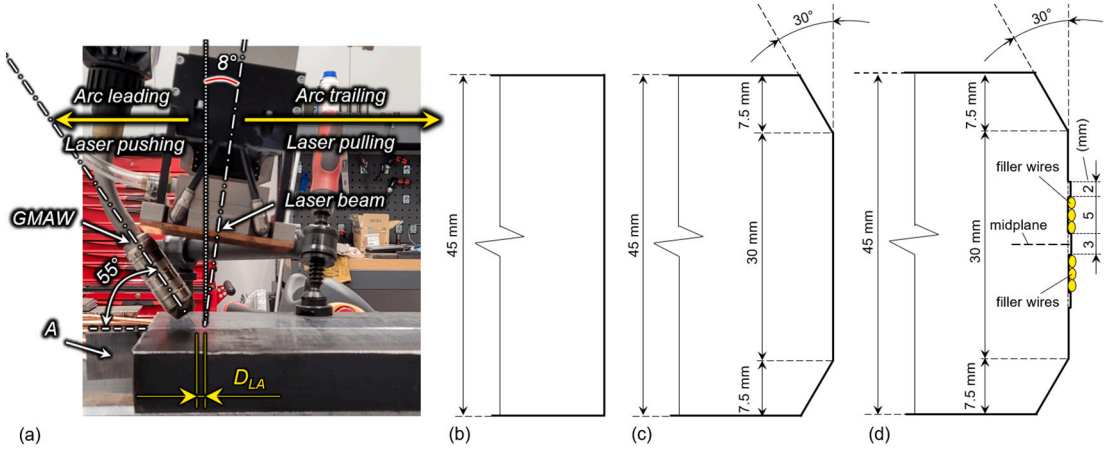

Fig. 1. (a) Experimental setup (D_{LA} is laser-arc interdistance, A is run-in welded plate). Groove preparation geometries: (b) straight I-groove; (c) Y-groove with straight edge; (d) Y-groove with steps and preplaced filler wires.

Table 1
Chemical composition (wt%) of the base plate and the filler wire based on producer's certificates.

Material	C	Si	Mn	P	S	V	Ni	Cr	Cu	Mo	Fe
BM[a]	0.04	0.08	1.97	0.007	0.001	0.01	0.70	0.07	0.18	0.1	Bal.
Filler wire	0.05	0.05	1.23	0.005	0.015	–	0.88	–	0.11	–	Bal.

[a] Contained small amount of Al, Nb and Ti (<0.03 wt%) and boron (<0.005 wt%).

Table 2
Mechanical properties of the base plate and the filler material based on producer's certificates.

Material	Yield strength, $R_{p0.2}$ (MPa)	Ultimate tensile strength, R_m (MPa)	Break elongation, A_5 (%)
BM	522	629	23
Filler wire	496–544	572–593	26

2.2. Microstructure and non-metallic inclusions

The WM and the HAZ in thick plates are large areas to cover. Therefore, the microstructure was studied based on the penetration depth of the first/second pass from the upper surface: 10—25 % depth representing the arc area, 50 % depth representing the middle of WM, 75 % depth representing the beginning of the root area, and 90—95 % depth represents the deep root area. The root area has the highest interest due to the numerous challenges. The samples were prepared using standard (EN ISO 17639:2003) metallographic preparation routines including grinding and polishing, followed by etching with a 2 % Nital solution for 10—20 s. The microstructure was studied by optical microscope and field emission scanning electron microscope (FEG-SEM, Zeiss Ultra 55) using 20 kV acceleration voltage. SEM is compulsory to recognize complex steel microstructures such as lath martensite and bainite. The polished and etched samples were studied by SEM with backscattering detector (for elemental contrast) and energy dispersive spectroscopy (EDS) to study NMIs. A point counting method as described in ASTM E562 was used to estimate the fraction of AF.

Table 3
List of process variables. Designation of welds is based on the groove type (I/Y shape), arc position (L is leading, T is trailing), preheating (P means it was used) and preplaced filler wire (W means it was used). Weld I-LP had preheating to 240 °C prior to the first pass. Weld Y-WP had preheating to 170 °C prior to the first pass with preplaced filler wire.

Weld designation/ pass	P_L	Groove type	Welding speed, m/ min	Air gap, mm	*WFR*, m/min (current, A/voltage, V)	Arc position	Q_L, kJ/ mm	Q_A, kJ/ mm	Q_H, kJ/ mm
I-L/1	15	I	0.8	1.0	11.0 (320/29)	Leading	0.79	0.56	1.34
I-L/2	15		0.7		11.0 (320/29)	Leading	0.90	0.64	1.54
I-T/1	15	I	0.8	1.0	11.0 (320/29)	Trailing	0.79	0.56	1.34
I-T/2	15		0.7		11.0 (320/29)	Trailing	0.90	0.64	1.54
I-LP/1	15	I	0.8	1.0	11.0 (320/29)	Leading	0.79	0.56	1.34
I-LP/2	15		0.8		11.0 (320/29)	Leading	0.79	0.56	1.34
Y-N/1	13	Y	0.8	0.8	9.5 (300/28)	Leading	0.68	0.50	1.19
Fill pass	–		0.4		10.5 (320/28)	Pushing	–	1.08	–
Y-N/2	15		0.8		9.5 (300/28)	Leading	0.79	0.50	1.29
Fill pass	–		0.4		10.5 (320/28)	Pushing	–	1.08	–
Y-W/1	14	Y	0.8	0.8	10.6 (310/29)	Leading	0.74	0.54	1.27
Fill pass	–		0.5		12.6 (390/30)	Pushing	–	1.12	–
Y-W/2	15		0.8		10.6 (310/29)	Leading	0.79	0.54	1.33
Fill pass	–		0.5		12.6 (390/30)	Pushing	–	1.12	–
Y-WP/1	14	Y	0.8	0.8	9.5 (310/28)	Leading	0.74	0.52	1.26
Fill pass	–		0.5		13.8 (390/30)	Pushing	–	1.12	–
Y-WP/2	15		0.8		9.5 (310/28)	Leading	0.79	0.52	1.31
Fill pass	–		0.5		13.8 (390/30)	Pushing	–	1.12	–

2.3. Numerical modelling

Three-dimensional numerical modelling was performed using the finite element method (FEM) in a general purpose Abaqus commercial software (2021 version), using DFLUX subroutine (written in Fortran using Intel Parallel Studio V2019) to introduce and control the moving heat sources. The numerical model was used for calculation of the thermal field to extract the cooling times at different nodes to understand the thermal cycle during welding and for the correlation with microstructure and mechanical properties. A three-dimensional conical volumetric heat source was used to simulate the keyhole and Goldak double ellipsoidal volumetric heat source was used for the arc. The model consisted of 130,000 finite elements using eight-node linear heat transfer hexahedral bricks (DC3D8). The mesh was finer close to the weld centerline to increase accuracy of the thermal field and to reduce calculation time. Using a conventional laptop (Intel Core i7-9850H, 2.60 GHz, 6 cores), the simulation of 50 s of welding time was completed in ~5 h using parallelization technique. Other data of the simulation technique and modelling data can be retrieved from [27].

2.4. Destructive and X-ray testing

A comprehensive destructive testing program was employed to assess the mechanical properties of produced materials. Vickers microhardness test was performed based on ISO 22826:2005 in accordance with ISO 6507–1:2018. The selected load was 500 gf ($HV_{0.5}$). Charpy V-notch (CVN) impact toughness testing was performed in accordance with EN ISO 9016:2012 and dimensions of specimens were 55 × 10 × 10 mm^3 with a standard notch geometry. Testing temperature was −50 °C. The minimum impact toughness is achieved when the notch edge is located perpendicular to the weld seam. This provides a fracture crack propagation path/plane that is parallel to the welding direction, causing easier delamination. The orientation of impact toughness specimens is designated as T-L type. For the WM, the notch was located at the centerline, according to Fig. 2a (line A corresponds to the notch edge). For the HAZ, the notch was located to cover the welds on both sides, see line B. This also includes the reheated unaltered coarse-grained heat-affected zone (UCGHAZ) and the intercritically reheated coarse-grained heat-affected zone (ICCGHAZ). A representation of different HAZs in double-sided LBW/LAHW is shown in Supplementary Data 1.

Micro X-ray computed tomography (μCT) was used to detect internal weld imperfections (or defects) such as porosity, cracking, and lack of fusion. Specimens were cut from the weld with an 8.5 mm width to increase the scan accuracy and detect small weld imperfections, see Fig. 2b. Nikon HT225 microfocus CT-scanner performed scanning at 225 kV and an X-ray tube current of 125 μA. During scanning, the sample was rotated by 360° in fine angular increments and a radiographic image was taken at each angular position. Scans were set at a slice thickness (or voxel size) of 0.0296 mm resulting in 2160 projections (or individual images) per sample. The raw data as a stack of images was post-processed using *Fiji* (based on *ImageJ*) open-source software with native functions and specialized plugins.

3. Results and discussion

3.1. Weld characterization using I-groove

I-groove beveling is the simplest edge preparation that offers fast and cheap welding implementation since no groove is needed to be milled. Therefore, it was initially used for understanding the process behavior and its limitations. The transversal macrosections of I-groove welds are shown in Fig. 3. The welds had lack of penetration (2—4 mm) in the middle of the plate. Lack of penetration from both sides provided unacceptable quality of the welds due to the lack of fusion that provided excessive solidified melt expulsion, or root gap sagging. According to the X-ray scanning, porosity and solidification cracks were mainly observed at the weld centerline (see Supplementary Data 2). Altering welding parameters had no significant effect on defect number and density. Both porosity and cracking could be related to a high depth-to-width ratio of the weld, a geometrical factor that will be discussed later in detail. The trailing arc (weld I-T) provided a slightly wider fusion zone on the top and lower penetration depth. Preheating provided much wider HAZ and no improvement in penetration depth.

Based on the hardness results (see Fig. 3), the arc area had hardness <280 HV for both WM and coarse-grained heat-affected zone (CGHAZ) due to slow cooling time $\Delta t_{8/5} > 7.0$ s regardless of welding parameters, see the numerically estimated values in Fig. 4. Notably, the hardness in the middle of BM is 210 HV and is slightly higher at subsurface regions, i.e., 230 HV. In the root (at 90 % depth), a hardness of 300 HV was achieved due to the high cooling rate. The hardness values were highest (> 320 HV) in the deepest areas of the root at the tip of maximum penetration depths. However, these areas are comparatively small and international standards do not indicate the necessity to measure hardness in these specific areas. The maximum allowed hardness in a weld is subtle and depends on many factors such as steel grade and field of application. Therefore, the values may vary significantly. According to DNVGL-OS-C401, the maximum acceptable hardness for the selected steel is 420 HV_{10}. Based on NORSOK M-101, the maximum hardness must be <350 HV_{10}. The hardness values are correlated with the amount of formed martensite that is susceptible to cold or hydrogen cracking. Therefore, the hardness should be minimized as much as possible and it

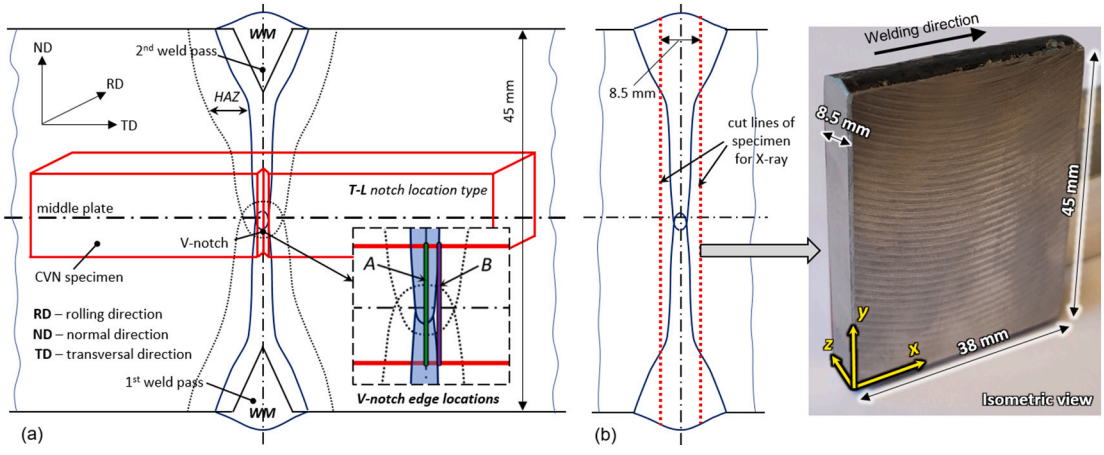

Fig. 2. (a) Location of CVN specimens at weld metal centerline *A* and at fusion line *B* on both welds including reheated zones. (b) Specimen extraction for X-ray computed tomography.

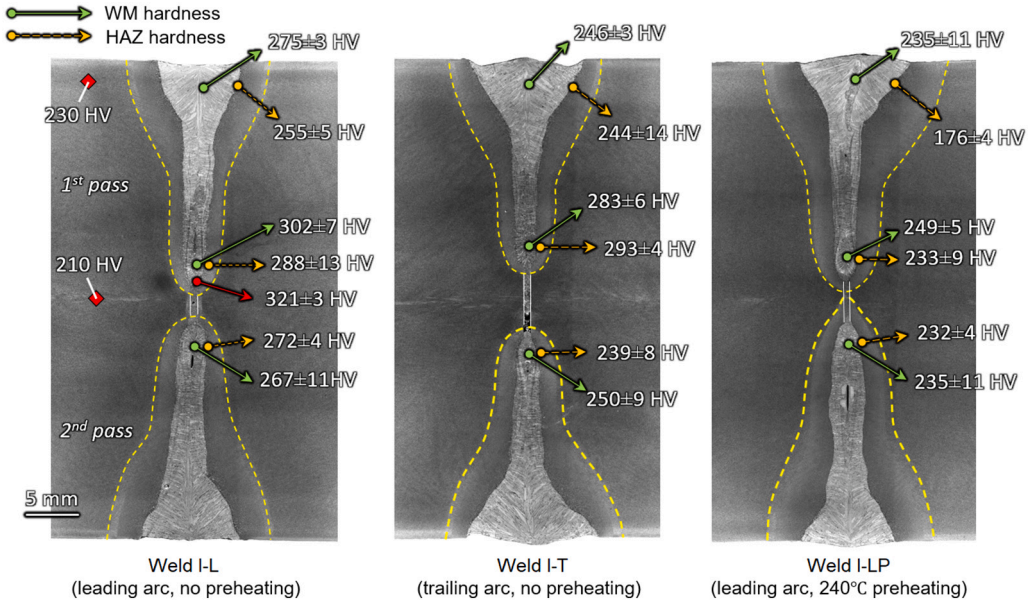

Fig. 3. Transversal macrosections of welds using I-groove preparation and microhardness results. Dashed lines indicate HAZ geometry.

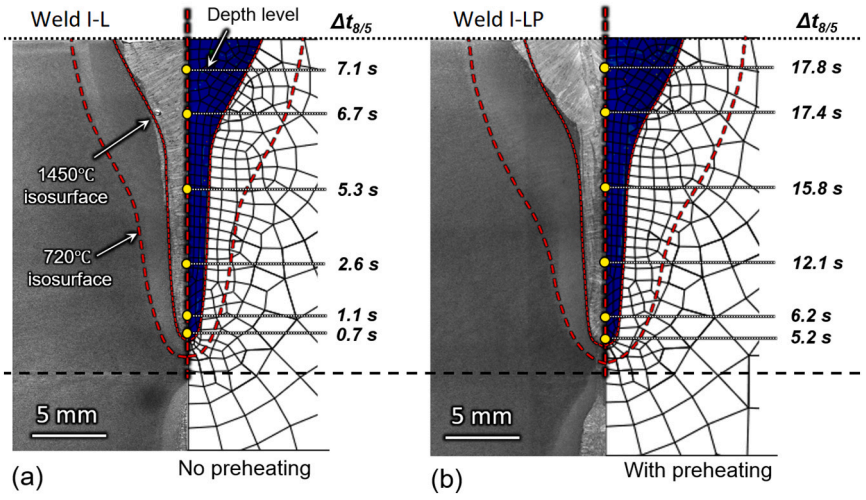

Fig. 4. Numerical simulation results of cooling time $\Delta t_{8/5}$ for I-groove welds (a) standard LAHW without preheating and (b) weld with preheating.

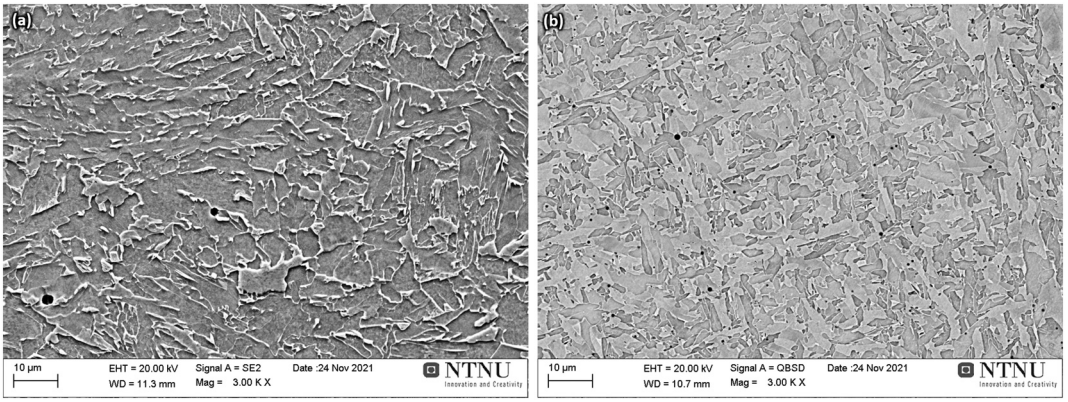

Fig. 5. (a) SEM of base metal representing granular bainite consisting of irregular ferrite plates (large gray platelets) with secondary phases between them. Few large NMIs can be observed (round-shaped black areas). (b) Backscattered SEM image of typical microstructure in arc area in all welds showing fine-grained AF nucleated at NMIs.

should not exceed the values found in the BM. According to the numerical simulation results, there is an ultra-fast cooling time of $\Delta t_{8/5} =$ 0.7 s in the root. After the first weld pass, the temperature of the plates was 90—100 °C (as measured) due to a substantial heat input (1.34—1.54 kJ/mm) from the arc and laser beam. Therefore, the root hardness for the second pass was reduced. The preheating of 240 °C prior to welding (with the similar as measured temperature prior to the deposition of the second pass) successfully reduced the hardness in the root areas by increasing the cooling time $\Delta t_{8/5}$ to 6.2 s. However, near the plate surface a prolonged $\Delta t_{8/5}$ to 17—18 s resulted in CGHAZ with a softening of 20 % from BM, which may reduce the overall weld strength.

The BM microstructure consisted of granular bainite (GB) which represents irregular (or quasi-polygonal) ferrite with second phases (bainite and retained austenite) distributed between ferrite grains [33], see Fig. 5a. The BM contained a low amount of NMIs with a typical size of 1—3 μm. Regardless of welding parameters, the arc area was characterized by large prior austenite grains separated by grain boundary ferrite (GBF), some Widmanstätten ferrite (WF), and a high volume fraction of AF (70—80 vol%) as shown in Fig. 5b. The AF was fine-grained in the arc area providing excellent toughness. Therefore, the arc area near the upper surface was not considered for toughness measurements. A high volume fraction of AF was formed at depths up to 50—60 % with slightly increased GBF, WF, and upper bainite (UB). At 75 % of the depth, the microstructure was altered significantly. The welds without preheating (i.e., weld I-L/I-T) predominantly consisted of UB with lath martensite (LM) whereas preheating (weld I-LP) provided more AF, GB, and a lower amount of UB. A similar trend was seen in the root of the weld (90—95 % of the depth), see Fig. 6. In the standard LAHW, lower bainite (LB) was identified by SEM which is recognized by carbides within bainitic plates. Furthermore, some fraction of AF had a different morphology compared to the arc area (see Fig. 5b), which resembles intragranular Widmanstätten ferrite (IWF) nucleated on NMIs dispersed within PAGs [34]. IWF nucleates heterogeneously on NMIs as one or two ferritic platelets and is characterized by a smaller width with significant elongation. This may provide lower misorientation angles compared to the fine-grained AF [17] resulting in lower toughness. However, IWF still possesses respectable toughness compared to bainite, due to the idiomorphic or equiaxed nature with a large crystallographic scatter [35]. The weld with preheating provided more fine-grained AF (~45—50 vol%) at root depths. The microstructure on a macro-level at large depths was characterized by smaller PAGs and few NMIs due to a poor filler wire transportation and fast cooling rate at this site, and this provided a limited time for growth of ferritic platelets. This induced a shift towards bainite formation. Since the size of the PAGs and the amount of NMIs may vary, there is a variety of different microstructures (also by volume fractions). Therefore, the root area is the weakest part of the WM due to low toughness and will be studied further. There are many factors for potent nucleation of AF: size of PAGs; number, size, chemical composition, morphological features, and dispersion of NMIs; cooling rate of transformation; thermal strain during solidification; and lattice mismatch. These factors mainly depend on chemical composition of the BM and the filler wire and on welding parameters which have the effect on cooling rate. Arguably, the main two factors are (*i*) PAG size and (*ii*) a density of NMIs. Therefore, the mentioned factors should comply with welding parameters for AF nucleation and growth to achieve >70—80 vol%. It has been shown [27] that there is a gradual decrease in AF vol% towards the root with a corresponding decrease of the $\Delta t_{8/5}$ cooling time.

The CGHAZ of the weld I-L without preheating ($Q_H = 1.34$ kJ/mm) mainly consisted of a mixture of UB and LM with some GB in the arc area, see Fig. 7a. In the root, the size of bainitic and martensitic laths decreased within smaller PAGs. Preheating provided larger PAGs at any depth due to a significantly increased cooling time $\Delta t_{8/5}$ by a factor close to three at depths up to 50 %, see Fig. 7b. In the root area, this factor was

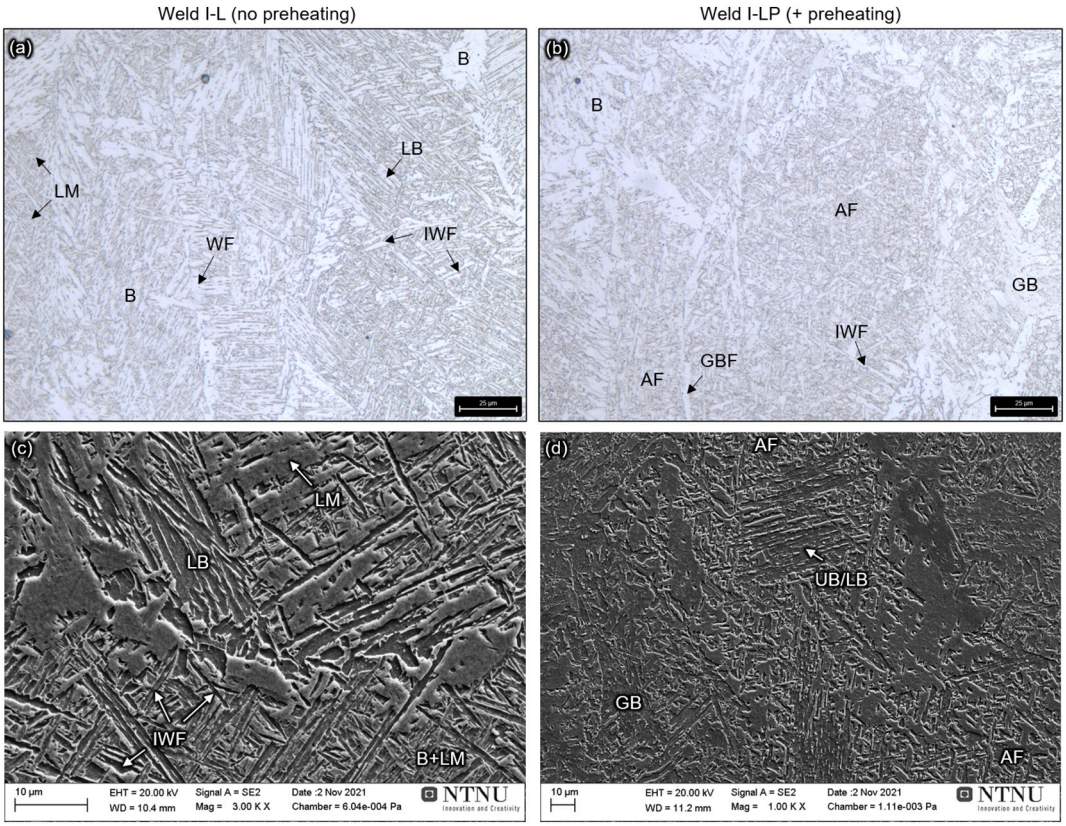

Fig. 6. (a, b) Optical micrographs of WM in root for weld without preheating and with preheating and (c, d) and SEM, respectively. Designation of microstructural constituents is indicated in the list of abbreviations.

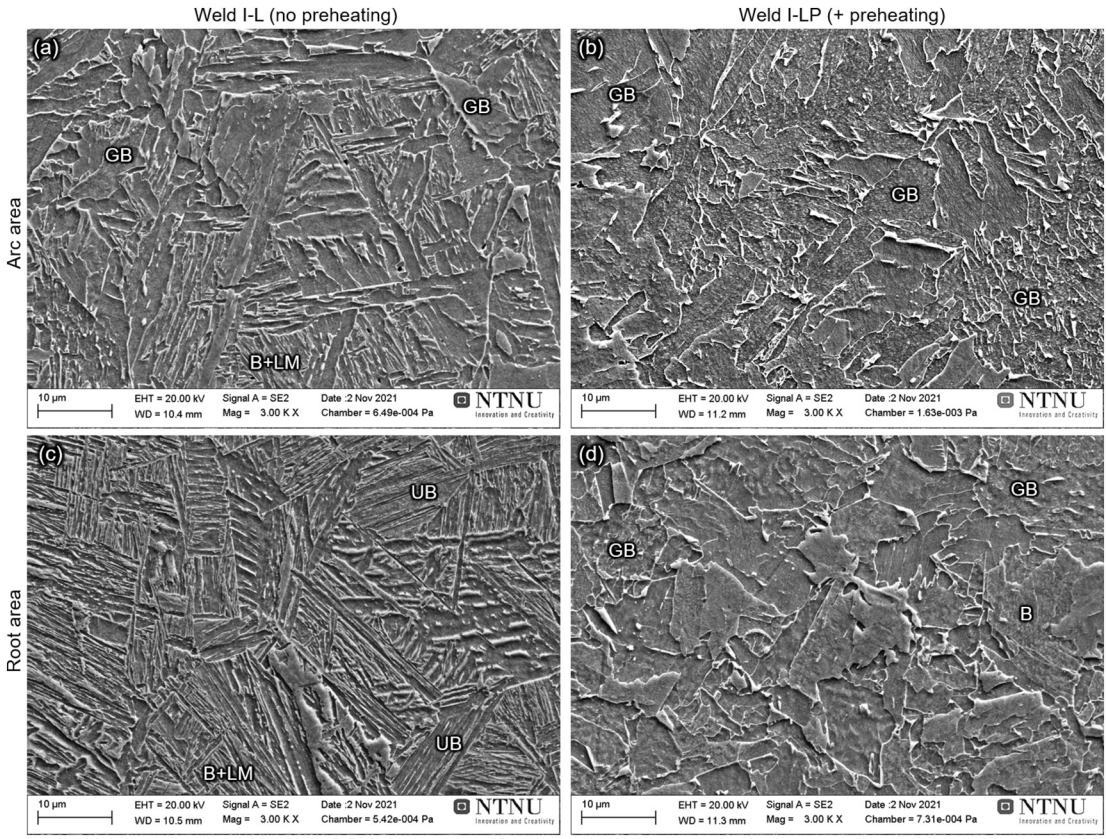

Fig. 7. SEM images of typical microstructure of CGHAZ near arc zone for weld without preheating (a) and with preheating (b), and in the root (c,d) respectively.

even higher (see Fig. 4). Therefore, it can be assumed that the energy input for the preheated weld is $Q_H \approx 4.02$ kJ/mm near the arc zone based on the $\Delta t_{8/5}$ values. Coarse grained granular bainite was formed and the secondary strengthening phases changed from thin continuous films (with platelets) into a more spheroidized morphology (blocky martensite-austenite islands) mainly located between GB grains. These factors may reduce the toughness, hence the preheating temperature should be reduced. When performing CGHAZ simulations by a Gleeble of a similar steel (microalloyed X100 with 0.07 wt% C), You et al. [36] found that the optimal heat input was 2.0 kJ/mm and sharply decreased when higher heat inputs were used. Moreover, higher heat inputs provided higher fraction of martensite-austenite (M-A) islands and low density of high angle grain boundaries. According to Cao et al. [37], who studied a similar steel alloy, lower heat inputs provided a smaller bainite packet size with an effective fracture crack arrestment within small sized PAGs. Furthermore, misorientation angles of blocks and packets were higher using lower heat inputs. Wang et al. [38] presented similar conclusions. Zhou et al. [39] indicated that higher misorientation of grains and block boundaries were significantly more effective in suppressing the secondary crack propagation.

3.2. Weld characterization using Y-groove

Based on the experimental results with the I-groove, it was challenging to achieve a full penetration and welds had many internal imperfections. Therefore, the experiments continued using the Y-groove beveling. A full penetration was successfully achieved due to a reduced 'effective thickness' of the plates since much less BM is needed to be melted. The transversal macrographs of these welds are provided in Fig. 8. The macrographs were taken from the beginning and end of the welds showing a consistent penetration depth which is of high importance. The post-processed X-ray micro-CT results are presented in Fig. 9 showing internal imperfections. The approximate maximum penetration depth is reflected by the dotted red lines. Here, the projections of all imperfections are shown after a certain manual post-processing. The data was post-processed in *Fiji* using the Volume Viewer plugin. Such method may obscure some small details of imperfections but provides an excellent overview and easy estimation of their fractions. To determine small details of imperfections, simple images and/or image stacks were used. Many thin cavities are clearly visible in the weld root. Their typical thickness (or width in transversal direction to the welding) is 400—600 µm. These cavities represent hot (or solidification) cracks. Their morphology is inconsistent in size but most of them have the shape of a 'boomerang' and the size is larger in the deposited second passes. Similar cracks were observed for the I-groove welds. A close examination of a hot crack is shown in Fig. 10 and clearly shows the presence of microcracks which are small and discontinuous with 350—450 µm in length along the transversal direction (the image stack is available as Supplementary Data 3). In welds with preplaced filler wire, cavities formed during the first pass were remelted by the second pass. There is also a certain periodicity pattern of their occurrence. Similar observations were shown by Wiklund et al. [10] but the study was based on transversal macrosections and without any X-ray detection. It is assumed, that the cracks are formed mainly due to excessively rapid cooling during the last stage of solidification (where the fraction of solid metal is in the range of 0.90—0.95). Such high cooling rates provides (*i*) a rapid grain growth from both sides that generates a lack of fusion at the weld centerline, (*ii*) hard brittle phases within the area, and (*iii*) high tensile stresses/strains [9,40]. There are also metallurgical factors of hot cracking such as (*i*) the grain size and morphology within weld centerline [41]; (*ii*) misorientation angles of grains; (*iii*) segregation of harmful elements (i.e., sulfur); and (*iv*) the existence of the secondary phases. Moreover, there is also a geometrical (shape) factor of deep welds for cracking formation where the root shape of a weld can be converging [10], diverging, and may include bulging regions due to complex melt flows [42]. In this work, all the welds had a similar shape of converging

geometry, thus no difference was found. The microcracks were frequently observed to be formed at the outer surfaces of the large cracks on both sides. Moreover, they continued to propagate from the end of cavity. Therefore, the microcracks showed some relationship with the shape of cavities. Some microcracks were also formed outside cavities.

Pores were formed at similar depths as solidification cracks (70—80 % of the maximum penetration depth) and they were frequently infused within large cavities. A moderate amount of pores were formed outside the weld centerline. According to ISO 12932:2017 applicable for the LAHW of steels, a fraction area of porosity and other defects is estimated as a projection on the cross-sectional weld area, not as a volume. To qualify for the level B stringent quality, the total area of pores must be <1 % for a single-pass and <2 % for a multi-pass weld. However, the minimum distance between pores should not exceed 3.0 mm. Large cracks (defect no. 100, ISO 6520-1) are not permitted as well as microcracks (defect no. 1001). Large solidfication cavities are not well described by relevant standards. However, they can be described as: (*i*) elongated cavities (defect no. 2015/2016) < 2.0 mm; (*ii*) non-fused area in weld metal (defect no. 401/4012) which is not permitted. Based on this data, all the welds made in this work cannot be qualified for the level B quality but could be qualified by eliminating cracks, microcracks, and clustered pores.

The statistical results of internal imperfections are shown in Fig. 11. The standard LAHW showed a high amount of porosity (area fraction of 1.33 %) and cracks (area fraction of 2.79 %). Moreover, the number of detected pores approached 500 counts. In the case of the preplaced filler wire, the amount of porosity was reduced substantially, to 0.52 % by area, but only marginally reduced the presence of cracks (to 2.03 %). Preheating in combination with preplaced filler wire slightly reduced the porosity content. Furthermore, it had a slightly adverse effect on cracking. As a result, a prolonged cooling time had little influence on the stress/strain field at such depths within the selected parameter range. The formation of pores can be explained through complex thermal fluid flow dynamics in the keyhole LBW. It is a quasi-stable state of ultra-high laser power melting where a few disruptive events may occur due to several phenomena such as (*i*) an excessive deformation of the rear keyhole wall in the form of small bulges caused by laser rays reflected from the front keyhole wall [27]. (*ii*) Instability due to a large vapor plume above the keyhole with high exerting speeds from the keyhole (>100 m/s [43,44]) with rapid oscillations that may inconsistenly absorb an incident laser beam. (*iii*) Uneven distribution of laser energy at the keyhole wall and variation of keyhole radius [45] that may cause high frequency fluctuation of the keyhole [46]. (*iv*) Turbulent melt flow with high speeds (> 12 m/s [47]) in the root area which may be caused by the aforementioned factors. These events may lead to a complete keyhole collapse that generates larger pores in consideration of high penetration depths. As a result, the bubbles cannot escape the weld pool on time and are captured by the solidification front. In the case of LAHW, the process is more intricate due to additional forces from the arc. A higher heat input from the laser beam and/or the arc may increase the width of the fusion zone, thus improving the degassing effect to mitigate porosity.

The measured microhardness in the arc area was slightly higher than found in the BM, see Fig. 12a–c. Microhardness was measured as a horizontal line near the surface with small steps (0.25 mm), revealing a softening in the FGHAZ/ICHAZ. No significant hardening was detected in the root areas. Higher hardness was detected in the weld Y-W, compared to the weld Y-N, due to a higher penetration depth and faster cooling time of 0.9 s based on the numerical simulation (see Fig. 13a). Preheating of 170 °C (weld Y-WP) widened the FGHAZ and ICHAZ with a slight softening. However, the softening was much less severe compared to the 240 °C preheating temperature (see Fig. 3). The preplaced filler wire combined with the 170 °C preheating was effective in mitigation of high hardness in the root since the cooling time $\Delta t_{8/5}$ was significantly prolonged to 2.4 s, similarly to the I-groove case (see Fig. 4).

A similar microstructural trend was observed up to 75 % of the depth for the Y-groove welds as for the I-groove welds. A low volume fraction of AF (20—25 vol%) was observed for the standard LAHW at 75 % depth within the WM. Preplaced filler wire raised the AF content to 35—40 vol %. The preheating provided an increase of AF to 55—60 vol% with a low bainite fraction (see Supplementary Data 4). The microstructure in the root (90—95 % depth) is shown in Fig. 14. The standard LAHW (the weld Y-N) showed the predominantly bainitic microstructure with lath martensite (Fig. 14a–a_i). Some AF was formed within fewer prior austenite grains and reached 15 vol%. The weld with preplaced filler wire (weld Y-W) provided more active NMIs, increasing the AF content to 25—30 vol% (Fig. 14b). The weld with preplaced filler wire and preheating (weld Y-WP) provided a further improvement in AF nucleation (Fig. 14c) and changed the morphology from elongated IWF platelets to fine-grained AF, more similar to the arc area. However, the volume fraction of AF was measured to 40—45 vol% which is lower than needed for high toughness (i.e., minimum 60 vol% AF). Bainite rich areas (Fig. 14a_{iii}–c_{iii}) showed many inactive NMIs. Most NMIs were promoting one (or two) plate nucleation and growth that is more typical to IWF. NMIs were often enveloped by a ferritic platelet due to their small size [48].

The statistical analysis of the NMIs is presented in Fig. 15. In the arc deposited welds (the fill passes), the area of density (%) of NMIs was the highest with a mean NMI diameter of 0.42 μm. In the arc area of LAHW, the density of NMIs was significantly reduced which is related to a higher dilution of BM (60—65 %) compared to the arc welds (the fill passes) which had only 20—25 % dilution. The density of NMIs in the standard LAHW sharply decreased towards the root area in a linear manner (weld Y-N, Fig. 15a) and it is one of the main reasons for the low fraction of AF. The density of NMIs in the BM was 0.02 vol% and that is

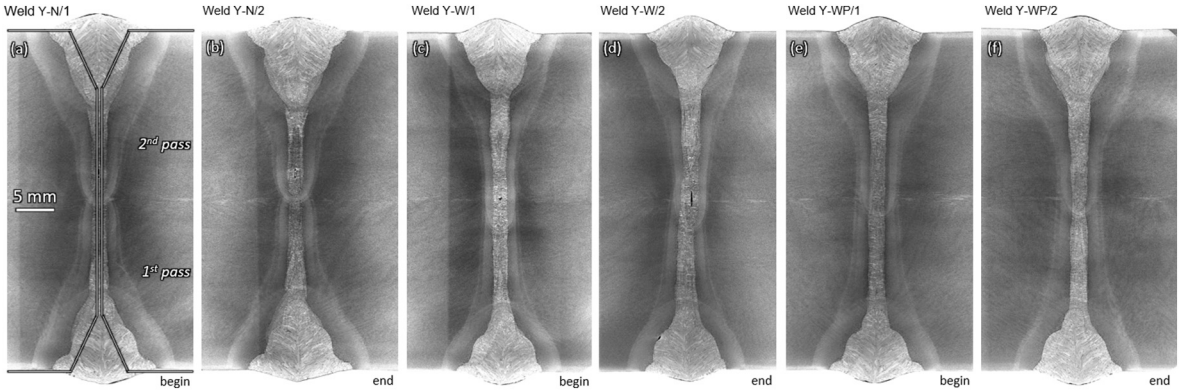

Fig. 8. Transversal macrosections of welds with Y-beveling and straight edge (a,b) standard LAHW, (c,d) preplaced filler wire without preheating, and (e,f) preplaced filler wire with preheating.

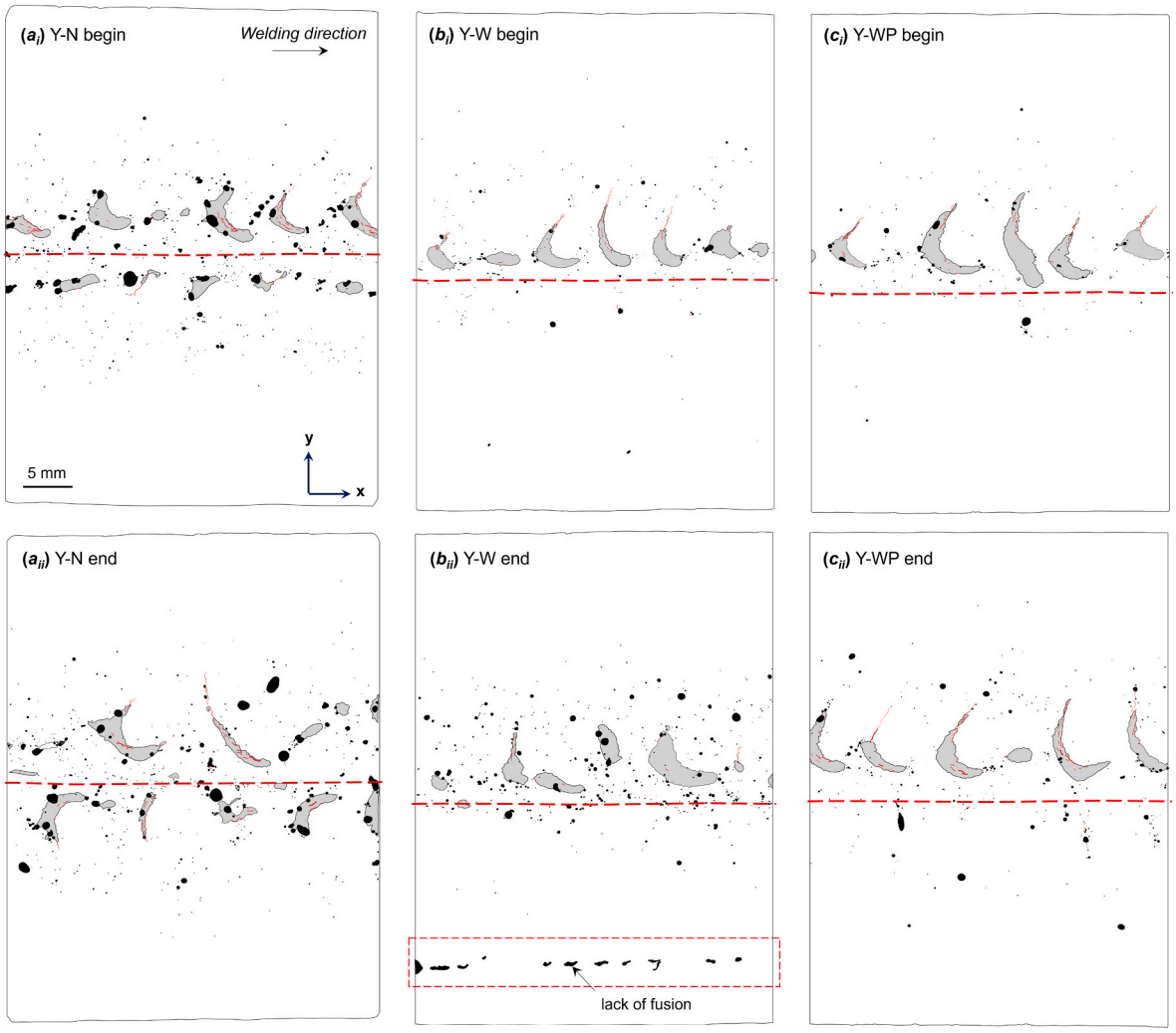

Fig. 9. Post-processed micro-CT results showing internal weld imperfections for Y-groove welds in *x-y* plane view: (a) weld without preplaced wire nor preheating, (b) weld with preplaced wire and no preheating, (c) weld with preplaced wire and preheating. Hot cracks are indicated as gray areas, transversal solidification microcracks are represented as red lines, pores as black areas, and approximate penetration depth limit of the second pass is shown as red dashed line. (For interpretation of the references to colour in this figure legend, the reader is referred to the web version of this article.)

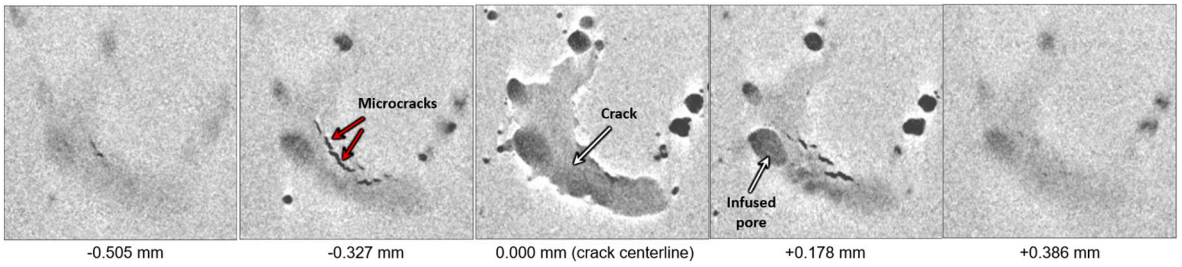

Fig. 10. Example of X-ray Micro-CT scans of different cracks at weld Y-N centerline within the fusion zone, view from *x-y* plane.

much lower than in the root of the standard LAHW. Therefore, some amount of the filler wire was transported to the root. Welds with preplaced filler wire (weld Y-W and Y-WP, Fig. 15b and c respectively) provided a higher density of NMIs in the root area. The diameter of NMIs decreased gradually towards the root showing a strong linear correlation. A similar trend showed a decreased cooling time towards the root (see Fig. 8). Since preheating has a strong effect on prolonging the cooling time $\Delta t_{8/5}$, it showed also a strong correlation on the diameter of NMIs. Therefore, the mean diameter of NMIs in the narrow laser welds can be estimated as a function of the cooling time $\Delta t_{8/5}$ (see Fig. 16). The typical average size of NMIs in arc welding, depending on heat input which directly controls the cooling time, is 0.33—0.70 μm for 1.0—8.0 kJ/mm heat inputs [49]. The mean diameter (d_v) can be estimated by the following relationship: $d_v = 0.35(0.8 \cdot Q_A)^{1/3}$. However, this estimation approach is not valid for the deep and narrow welds. According to Lee et al. [50] the optimal diameter of NMIs for a high probability of AF nucleation is 1.0—1.2 μm in low carbon steels (0.042 wt% C) welded by arc welding where a high oxygen-containing metal-cored filler wire was used. Seo et al. [51] reported a high probability of AF nucleation at NMIs with a diameter of 0.7 μm in C-Mn steels. In a previous work [32], where

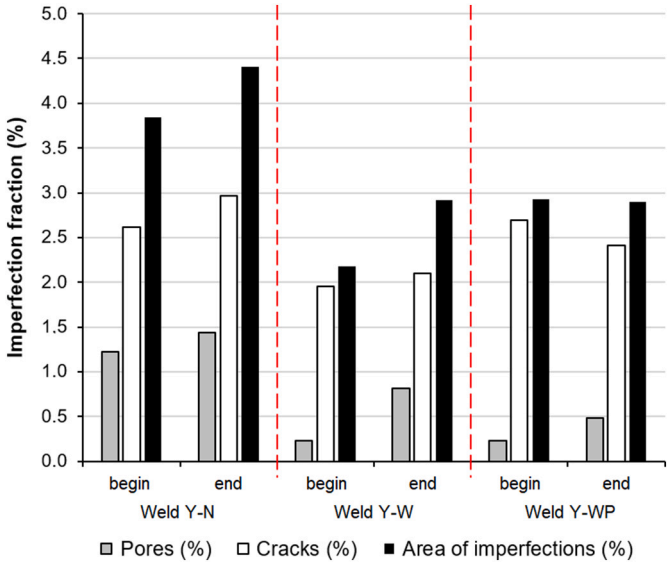

Fig. 11. Fraction of imperfections based on μCT scans. Area of imperfections is a combination of pores and cracks. Begin/end is location of extracted weld section in welding direction.

a different BM and preplaced filler wire were used, the mean diameter of NMIs was 0.37 μm at cooling times in the range of $\Delta t_{8/5} = 2.5$—3.2 s in deep roots. The density of NMIs was much higher (1.5—1.9 %) due to significantly lower dilution of the BM, only 18 %. However, a low fraction of AF was formed because the nucleation of ferritic platelets and their growth was impeded. This was related to the two factors: (*i*) inactive inclusions due to their unfavorable chemical compositions and (*ii*) excessive density of NMIs which may obstruct austenite grain growth through the Zener pinning effect, hence, reducing the size of PAGs. In another work [27], where the same BM was used without preplaced filler and with the similar BM dilution in the root comparable to this work, the mean size of NMIs and their density were similar to the values of the current work (~0.16 μm) for welds without preheating and preplaced filler wire. However, the NMI density was higher (0.12 vol%) since the penetration depth was lower with a better filler wire transportation to the root. This implies that there are many factors that may affect the characteristics of NMIs, which include: chemical composition of base metal and filler wire, process parameters that controls dilution and cooling times. The nucleation and growth of AF has a more intricate mechanism that also depends on many factors and an accurate prediction of the volume fraction is not yet available according to the authors' knowledge. Notably, an excessive amount of inactive (or inert) NMIs with a large diameter is harmful because they assist in void formation and growth during the mechanical loading [52]. Lan et al. [53] identified that with an increase in the size of NMIs beyond 1.0 μm, the critical fracture stress is significantly lowered for modern HSLA steels in both

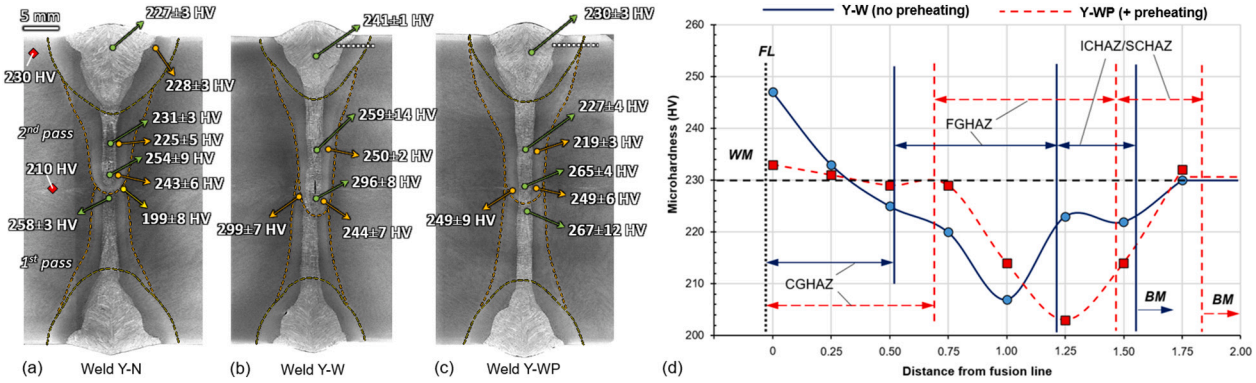

Fig. 12. (a–c) Microhardness results of weld with Y-groove with double-sided technique and (d) horizontal transverse line microhardness results in heat-affected zone of upper part of welds with and without preheating.

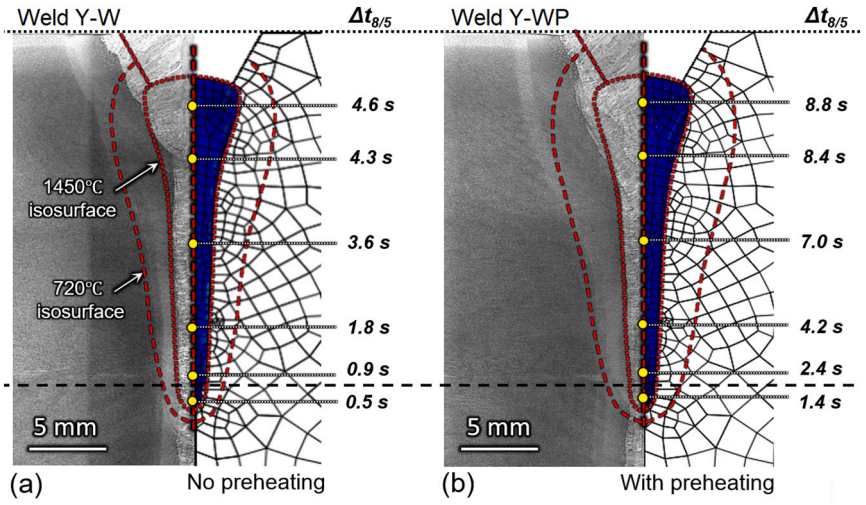

Fig. 13. Numerical simulation results of cooling time $\Delta t_{8/5}$ for Y-groove welds with preplaced filler wire in case of: (a) weld without preheating and (b) weld with preheating.

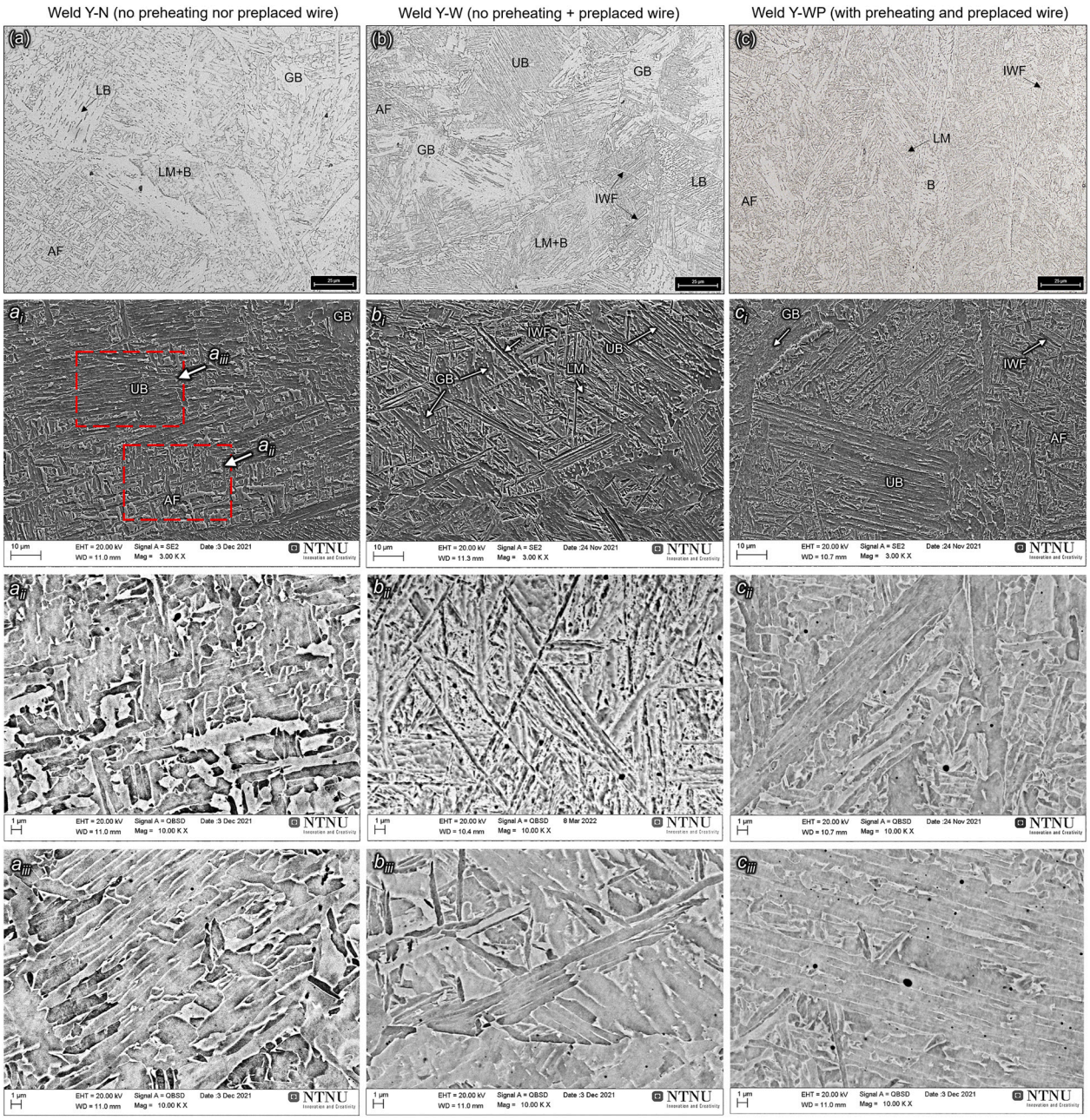

Fig. 14. (a–c) Optical micrographs of WM in the root area (95 % depth) for selected welds. (a_i–c_i) Low magnification SEM of typical microstructure. (a_{ii}–c_{ii}) High magnification SEM (in backscattered mode) of AF rich areas and (a_{iii}–c_{iii}) of bainite rich areas respectively.

the WM and the HAZ. Therefore, the optimal size of NMIs should be within the range of 0.45—1.0 μm to avoid cleavage fracture initiation.

The chemical composition of NMIs in the BM consisted of a complex combination of Al_2O_3 core, Ti_xO_y, and MnS with TiN attached to a core (see Supplementary Data 5). Si was also detected which may form many potent NMIs such as $MnO{\cdot}SiO_2$ or $(Ti,Si)O_x$, and can be a part of more complex NMIs [21]. The fundamental principles of a complex NMI are described in [54]. The chemical composition of NMIs in the arc area was similar to the BM (see Supplementary Data 6) in all the Y-groove welds but with a higher concentration of Si and Mn inside the NMIs. Therefore, the formation of $MnO{\cdot}TiO_2$ (as a part of the core) is highly possible based on the EDS mapping which has high potency of AF nucleation. Another possible NMI with a high nucleation potency is $MnTi_2O_4$ [55].

In the root area, EDS detected only Al_2O_3 for both active and inactive inclusions. A few active NMIs were studied with EDS point scan, and then it was able to detect other elements. The EDS point spectrum of two randomly selected NMIs is shown in Fig. 17. A variation in the chemical composition of NMIs was observed. The observed NMI consisted of Al_2O_3 with Ti_2O_3 as a multi-phase core with galaxite ($MnO{\cdot}Al_2O_3$) which is a highly potent NMI with the Mn-depletion zone that serves as a driving force for nucleation of ferritic plates. Here, the formation of $MnTi_2O_4$ is also possible which is favorable for AF nucleation. Some other active NMIs had sulfur and no oxygen, thus consisted of simple MnS (with possible FeS) in combination with Mn-silicates and possibly some CrS. Therefore, most of inactive NMIs in the root area consisted of the basic Al_2O_3 core with a low nucleation potency for AF. This shows a strong relationship of the ultra-fast cooling time ($\Delta t_{8/5} < 1.0$ s) and the chemical composition of NMIs. There is a noticeable lack of titanium detected in the root area with the absence of nitrogen. These constituents, in the form of TiN, are highly potent for the AF nucleation and are attached to the core in the absence of silicates. The selected filler wire in this work provided Ti-containing NMIs in the arc area and NMIs in the

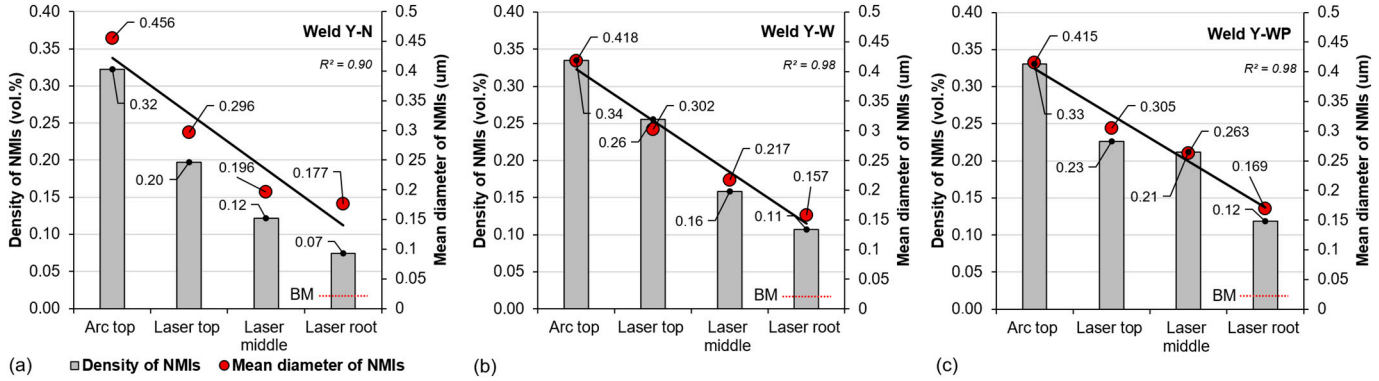

Fig. 15. Statistical results of NMIs in (a) weld Y-N without preplaced filler wire and preheating, (b) weld Y-W without preplaced filler wire with preheating, and (c) weld Y-WP with preplaced filler wire and preheating.

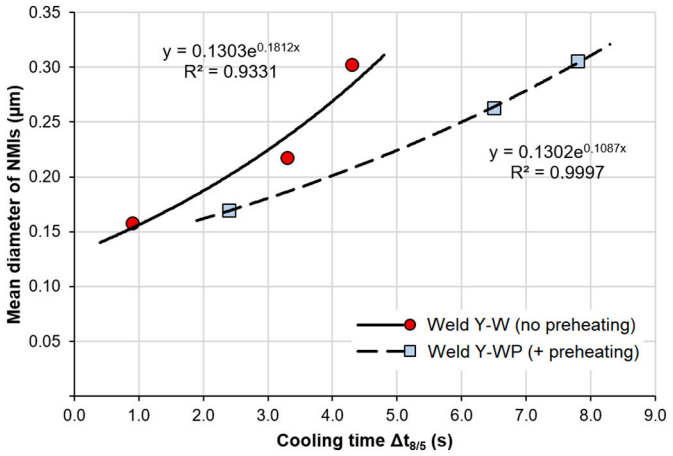

Fig. 16. Effect of cooling time on the mean diameter of NMIs in deep and narrow welds.

BM also contained Ti. A lack of AF in the root area may be due to Ti depletion within the weld metal matrix associated with ultra-fast cooling times, hence there is no time for Ti to form at NMIs. Titanium is one of the most potent elements for AF nucleation. Evans [56] reported an increase in the AF content to 75 % with additions of 30—40 ppm Ti at low Al level (< 60 ppm) and at 450—470 ppm oxygen. Seo et al. [51] showed that a high AF fraction can be achieved by adding >400 ppm of Ti in multi-pass arc welding. Later, it was claimed that a minimum of 9 ppm of Ti is needed to boost the fraction of AF from 5 % to 70 % in low carbon C-Mn steel at 3—16 ppm of Al [57]. The difference in results can be related to the oxygen and Al levels within the WM. However, excessive Ti additions (>0.02 wt%) may decrease the formation of AF. Addition of Ti-nanoparticles provided a significant improvement in AF nucleation (at 0.02 wt% Ti) in multi-pass arc welding [58]. Dabiri et al. [59] reported an increase of AF (up to 75 %) and improved toughness by adding 0.023 wt% ZrO_2 nanoparticles. However, the behavior of Ti addition on AF formation under ultra-fast cooling times has not been reported yet. Another solution to increase the AF nucleation is to use a more adapted base metal, thus Ti-killed steel may provide improved weldability. As an example, Ti—Zr deoxidized steel improved the toughness by promoting ZrO_2·MnS inclusions [60]. Addition of cerium with sulfur in the BM promoted a high fraction of AF (up to 80 %) for autogenous LBW of 6 mm thick plates [61]. Development of the BM specifically for LBW has low viability, thus the addition of advanced elements via the filler wire is more promising option.

The CGHAZ microstructure for non-reheated areas near the FL was similar to the I-groove samples due to similar heat inputs. However, in the Y-groove case, a full penetration was achieved with a slight over-penetration in the root area. This provided reheating of the CGHAZ. In the unaffected (or super-critically reheated) CGHAZ (see Fig. 18), the microstructure consisted predominantly of bainite (Fig. 18a,b) for both non-preheated and preheated welds. In the latter case, the size of PAGs was slightly larger. A higher volume fraction of GB was formed in the ICCGHAZ and thin M-A islands as continuous films were formed at the grain boundaries of PAGs as shown in Fig. 18c,d. In addition, some M-A islands were present inside PAGs which can serve as a crack initiation point [62]. Such M-A formation may promote cleavage fracture,

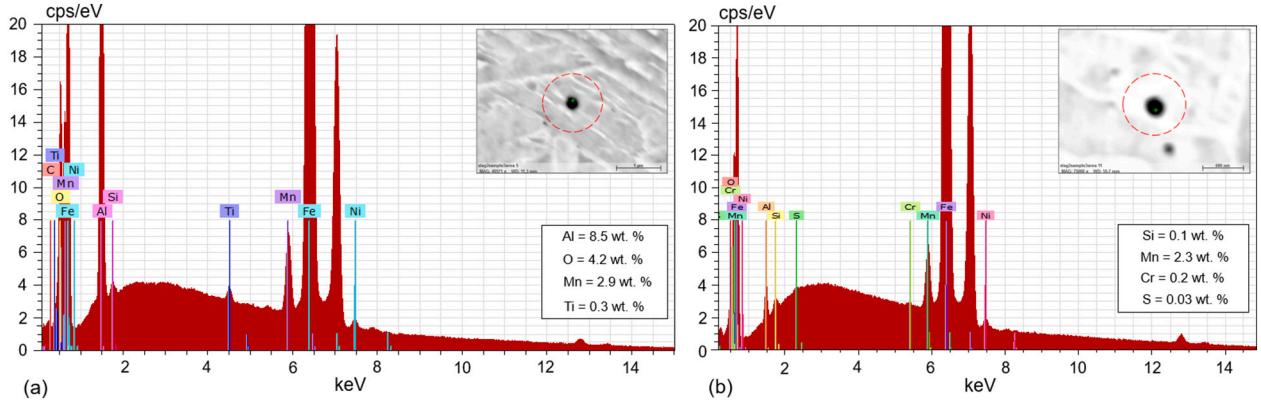

Fig. 17. EDS analysis spectra of two randomly selected active NMIs from root area (welds with preplaced filler wire) nucleated AF platelets under ultra-fast cooling time: (a) Ti-containing NMI (possible combination of Al_2O_3 core with/or $MnTi_2O_4$, $MnO{\cdot}TiO_2$, $MnO{\cdot}SiO_2$), (b) S-containing NMIs (possible MnS as core with CrS) with Mn-silicate.

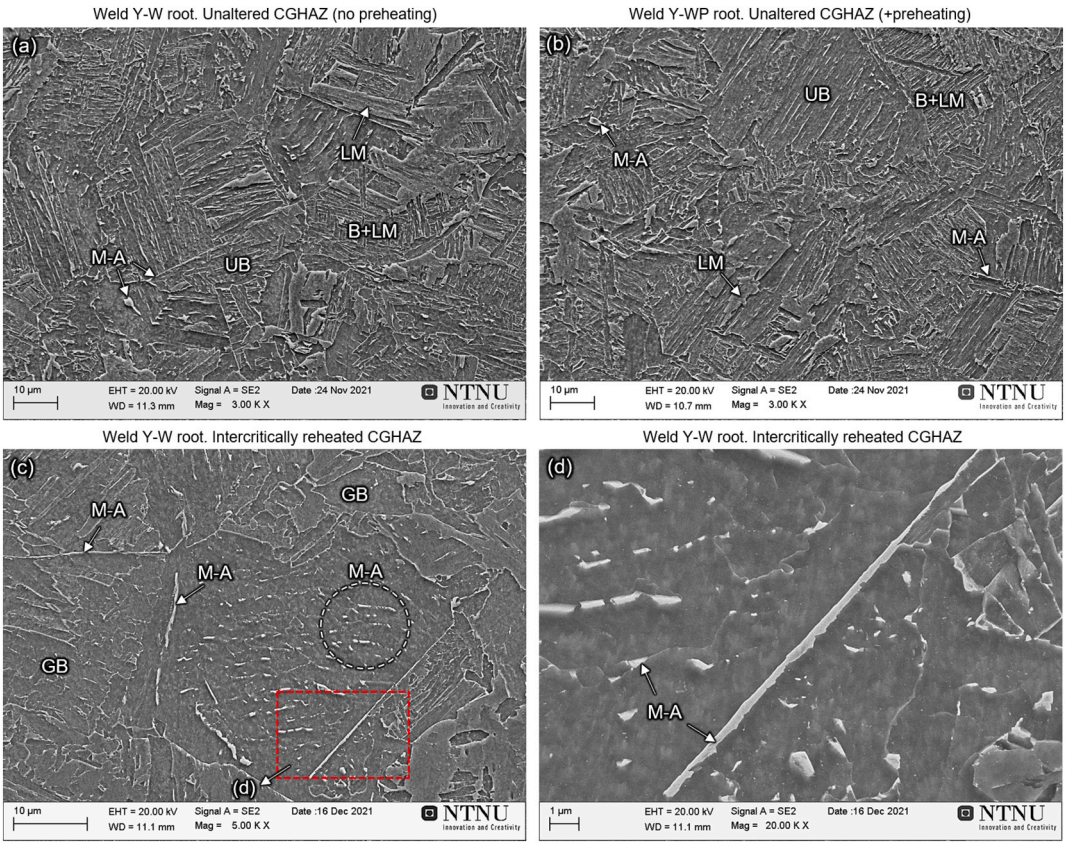

Fig. 18. SEM micrographs of HAZ in root for selected Y-groove welds: (a) unaltered CGHAZ without preheating, (b) unaltered CGHAZ with preheating, (c) intercritically reheated CGHAZ without preheating, and (d) high magnification of M-A formation at grain boundaries and small M-A islands within prior austenite grains.

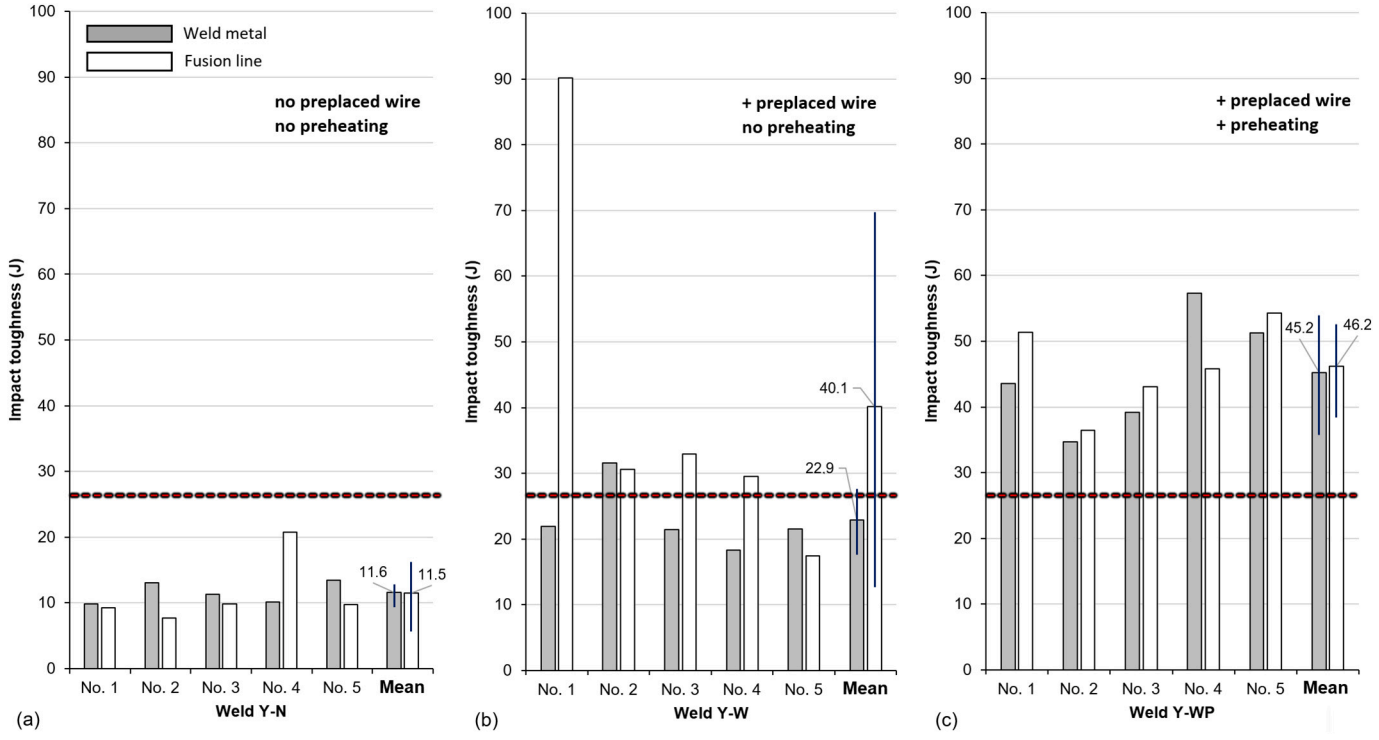

Fig. 19. CVN impact toughness values conducted at −50 °C of each individual sample (denoted as no. 1—5) and mean result for (a) weld Y-N, (b) weld Y-W, and (c) weld Y-WP. Minimum acceptable toughness value of 27 J is indicated by red dashed line. (For interpretation of the references to colour in this figure legend, the reader is referred to the web version of this article.)

especially when located at grain boundaries. A few M-A islands had a morphology of massive blocks as reported by You et al. [36] due to low reheating temperatures. However, most M-A phases were formed as small blocks (or granular), and/or as thin continuous films (as shown in Fig. 18d) due to fast cooling rates. Zhou et al. [63] indicated that refined retained austenite islands and thin films with their fine dispersion are effective in the crack arrestment mechanism in medium carbon steels, whereas blocky M-A had a detrimental effect and promoted cleavage fracture. In the subcritically reheated HAZ, the microstructure evolution was similar. Notably, in the intercritically reheated ICHAZ, large M-A islands were also detected with a twinned structure. It is believed that such morphology may also be harmful compared to M-A islands in the ICCGHAZ. However, the measured hardness in this zone was similar to the BM (see Fig. 12) and due to the small size area of ICCGHAZ zones and their low population, they may not be harmful for the toughness.

3.3. Impact toughness results

The CVN impact toughness results are presented in Fig. 19. The minimum acceptable toughness value is 27 J based on ISO 16834:2012 and DNVGL-OS-B101. Note, that the requirements for a toughness value depends on steel grade (tensile/yield strength), chemical composition, production method or condition, thickness of plates, application of external forces, and testing temperature. The standard LAHW (weld Y-N) exhibited a low toughness of 11.5 J at −50 °C as was expected due to much UB with LM (see Fig. 14). Inspection of the samples after testing revealed the appearance of cavities and hot cracks, in both WM and FL samples. In the latter case, the crack path deviates into a much weaker zone which is the WM, containing the large cavities. They appear to be similar in morphology to the defects detected by μCT, refer to Fig. 9. SEM inspection of the fracture surface from a selected CVN sample (see

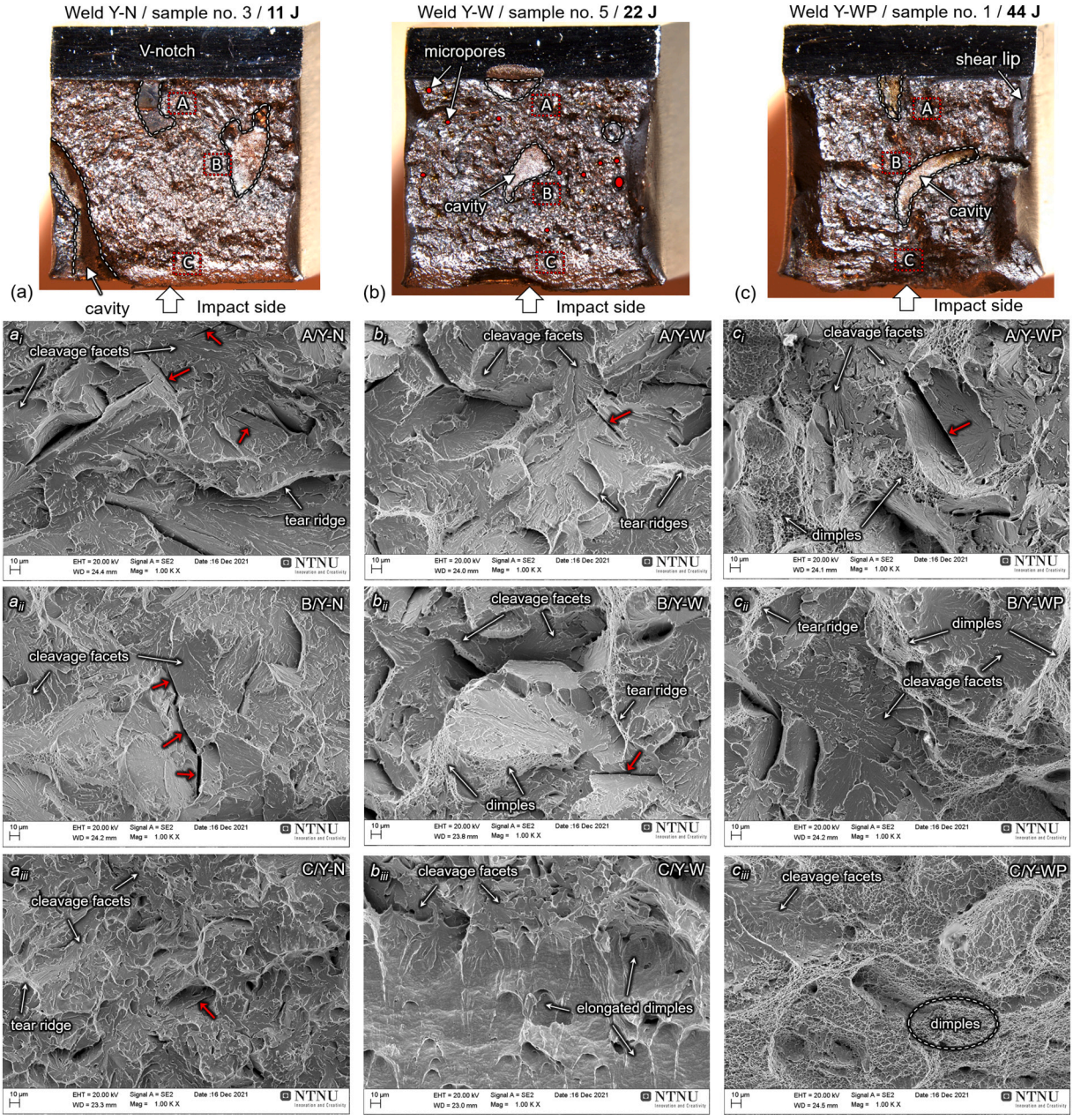

Fig. 20. SEM micrographs of fracture surfaces from selected Charpy samples in three areas where area *A* is fracture initiation zone, area *B* is unstable fracture propagation zone and area *C* is fracture end zone. Cavities (or hot cracks) are represented with dashed white lines. Red arrows indicate secondary microcracks. (For interpretation of the references to colour in this figure legend, the reader is referred to the web version of this article.)

Fig. 20a) revealed a brittle fracture mode by the quasi-cleavage mechanism. The fracture initiation zone (area A, Fig. 20a_i) was characterized by large cleavage facets and indicates a transgranular fracture. This indicates a rapid fracture propagation behavior with many secondary microcracks, indicated by red arrows. Dimples were infrequently observed in the unstable fracture propagation zone (area B, Fig. 20a_{ii}) which were located on the tear ridges. In the fracture end zone (area C, Fig. 20a_{iii}), the size of cleavage facets was significantly reduced with fewer microcracks, and more dimples were found on the thicker tear ridges. The quasi-cleavage fracture mode is common for different low carbon steels at low temperatures [64,65] and its transition, the ductile-to brittle transition temperature, can be shifted towards lower temperatures through microstructural refinement.

The weld Y-W with the preplaced filler wire and no preheating showed an improved impact toughness by a factor of two, from 11 J to 23 J, due to higher AF vol%. Therefore, some dimples were observed within the fracture initiation zone mainly located on the tear ridges with fewer secondary microcracks (Fig. 20b_i). However, it was still mainly controlled by the quasi-cleavage fracture containing many large cleavage facets. More dimples were found in the unstable fracture growth zone (Fig. 20b_{ii}). Large and elongated dimples, or primary voids, were formed in the fracture end zone (see Fig. 20b_{iii}) with fewer cleavage facets providing a ductile rupture.

Application of the preplaced filler wire with 170 °C preheating (weld Y-WP) provided a significant improvement in toughness in both WM and HAZ due to further enhanced AF vol%. All test samples provided minimum acceptable toughness of 27 J. Increased volume fraction of AF due to finely dispersed NMIs with a small in diameter resulted in a mixed brittle-ductile fracture in the fracture initiation zone and in the unstable fracture propagation zone (Fig. 20c–c_{ii}). The fracture end zone (see Fig. 20c_{iii}) showed a predominantly ductile or fibrous fracture mode characterized with many fine dimples, which indicates coalescence of microvoids. The effect of AF volume fraction on the toughness is presented in Fig. 21. It clearly shows an increase of the impact toughness with an increase of AF vol% with a strong linear correlation.

The SEM inspection of the weld Y-N with low toughness near the fracture of the Charpy specimen on the machined side surface, showed low plasticity and a transgranular fracture associated with upper bainite (see Fig. 22a) with frequent microcracks. The weld Y-WP with high toughness (see Fig. 22b) revealed plastic deformation near the fracture path due to higher AF volume fraction, and a few secondary microcracks. Moreover, plastic deformation of the fractured specimens is well correlated with the toughness values, see Supplementary Data 7. The weld Y-N exhibited minimum signs of plastic deformation whereas the weld Y-WP provided clearly visible plastic deformation.

Hot cracks directly affect the toughness since they reduce the load bearing area of the WM and provides a crack propagation path. The area of imperfections (or non-fused area) and its relationship with the toughness values is shown in Fig. 23. From the measured mean values (Fig. 23a), the welds with lower non-fused areas provided higher toughness. However, the effect of non-fused area based on the toughness of individual specimens showed a low correlation (see Fig. 23b). Some weak correlation was spotted for the weld Y-WP with preheating and preplaced filler wire. Therefore, the control of the fracture crack was mainly influenced by the microstructure while the non-fused areas weakly inferred the values and the results can be directly compared between different welding methods. Hot cracking should be eliminated and porosity minimized to increase toughness values further.

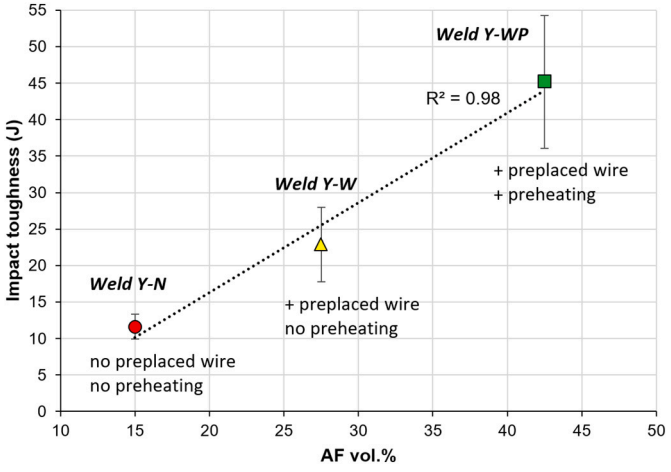

Fig. 21. Effect of AF vol% on impact toughness at −50 °C for Y-groove welds.

3.4. Summary of results and discussions

The experimental results imply that there are several challenges to be considered in deep welding of thick steels. The common issue with deep welds is a high hardness in the root. It was characterized by rapid cooling rates exceeding 300 °C/s within the cooling time $\Delta t_{8/5}$ using standard LAHW. The main microstructure observed was a mixture of bainite and lath martensite which has a poor toughness [66]. The filler wire distribution in deep and narrow welds is substantially limited and showed a linear sharp decrease towards the root. Therefore, only a small portion of the filler wire was delivered to this area and this provided a low density of NMIs. However, a high density of NMIs is compulsory for the nucleation of AF [17–19,31,34,35,48,54,55]. Optimization of process parameters may increase the filler wire transportation towards the root but is limited due to a narrow weld pool geometry and most of the filler wire populates the upper rear weld pool. The filler wire transportation to deep areas can be improved by a reduction in welding speeds at the expense of productivity. Alternatively, an increase of arc power with an increase of filler wire feed rate at the same time may improve a mixing and possibly reduce the BM dilution. However, an increase of arc power should be carefully assessed since it may: destabilize the keyhole [14], generate much porosity, enlarge the grain size [36,37] in the HAZ, and provide softening in the HAZ due to excessive heat input.

The potency of NMIs for the nucleation of AF is complex since it depends on many factors and conditions. In general, the favorable factors should be optimized to provide a high number of active NMIs [21]. This include: size, density, and chemical composition of NMIs, size of PAG, chemical composition of base metal and filler, processing parameters affecting the $\Delta t_{8/5}$ cooling time, and filler wire distribution with dilution. The cooling rate $\Delta t_{8/5}$ has a strong effect on the mean diameter of NMIs and is correlated well with the predicted values. The preplaced filler wire provided a notable boost in the density of NMIs, thus AF volume fraction increased. The preplacement of filler wire prior to welding is a compelling method to overcome issues with the filler wire distribution. It works well only on laboratory scale but may be difficult to employ on industrial scale. In addition, some NMIs in the root were inactive which was related to the changes in chemical composition and too small mean diameter for AF nucleation compared to the arc area which has slower cooling times. Moreover, faster cooling rates changed the morphology of AF which had elongated platelets nucleating intragranularly with possibly low misorientation angles. Preheating prior to welding showed a further enhancement in the volume fraction of AF in combination with the preplaced filler wire. An increased activity for the AF nucleation was associated with the prolonged cooling time $\Delta t_{8/5}$ that also slightly increased the mean diameter of NMIs. As a result, this significantly increased the toughness. The morphology of AF was slightly altered from elongated platelets to more refined AF. However, it was not possible to achieve a high degree of active NMIs with fine platelets and this may be related to the high cooling rates and insufficiently large diameters of NMIs. This indicates that the use of metal-cored commercial filler wire may not be optimal for such purposes and further improvements are required. One of the possibilities is to use

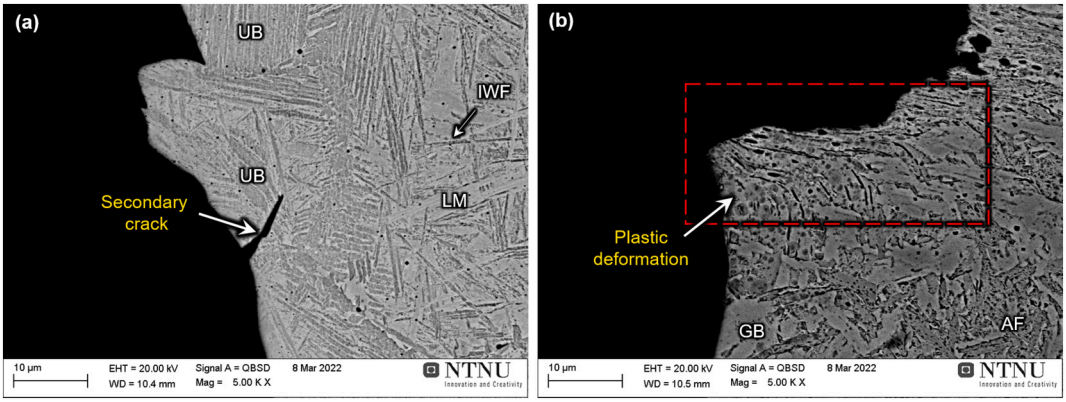

Fig. 22. SEM micrograph near the facture path in (a) low toughness weld Y-N and (b) high toughness weld Y-WP.

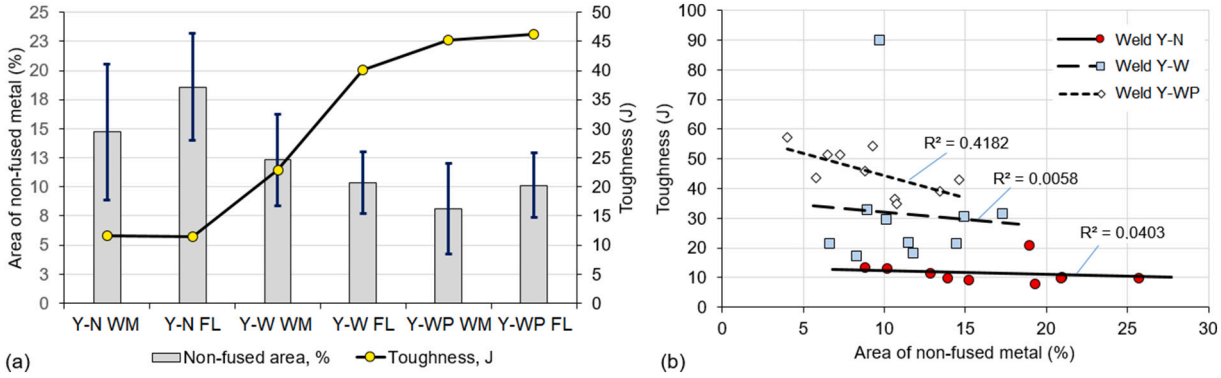

Fig. 23. Effect of non-fused areas (hot cracks and pores) measured from Charpy fractures samples on toughness: (a) general overview based on mean values and (b) for individual samples.

the addition of micro- or nanoparticles. However, this is a technologically challenging task due to safety issues and production method for small diameter (1.0—1.2 mm) solid or metal-cored filler wires.

Deep penetration LBW/LAHW has a quasi-stable keyhole condition with high fluctuations [46] and during solidification many pores may form. Here the application of preheating significantly reduced porosity. The welds contained large solidification cracks at the weld centerline and this imperfection is considered as critical and probably the most challenging to eliminate in deep welds. At this point, the exact mechanism of the crack formation is not discovered, and mitigation solutions have not been achieved. Preheating and preplaced filler wire had a low influence on crack formation. It is well known that solidification cracks are formed at much higher temperature ranges compared to the solid-state transformation temperature of most microstructures found in low carbon steels [42]. Thus, tougher microstructures cannot arrest the initiation of solidification cracking. High stresses/strains during solidification in the root area has a more important role, which exceed the yield strength of the mushy zone [40,42]. However, a higher formation of AF may suppress delayed cracking by the arrestment mechanism in the vicinity of brittle martensite with high hardness. Solidification cracks are also strongly correlated to the geometry of a fusion zone [10]. Therefore, a wider fusion zone may reduce stresses and strains with slower cooling rates. This can be achieved by reducing the welding speed, increasing laser power or increasing laser beam spot diameter, or using more advanced techniques such as laser beam oscillations. The latter technique may also refine the grain structure and stabilize the keyhole with a potential to reduce the porosity level at the same time. However, it requires advanced optical elements due to the thermal lensing effect at higher power densities of the laser beam. There are also other possibilities such as the use of a non-Gaussian laser spot profile, dual-laser or twin spot technique to change and manipulate the geometry of the weld pool.

According to the experimental results, it was shown that a higher fraction of AF is compulsory to achieve high toughness at low temperatures. Therefore, the standard LAHW may be not applicable since it does not provide a sufficient amount of filler wire to the root. Moreover, the cooling time $\Delta t_{8/5}$ is too fast for AF nucleation and growth, and a high dilution (up to 65 %) of the base metal reduces the density of NMIs. Higher toughness was obtained in welds with a higher AF volume fraction. Therefore, the toughness can be strongly controlled by the microstructure. Hot cracks have a detrimental effect on toughness which promotes the cleavage fracture and reduces the load-bearing area. Therefore, a further study is required for their mitigation. Solving the issue with (*i*) unfavorable microstructure and (*ii*) internal weld defects, especially related to large solidification cracks at the weld centerline; it is expected to have an excellent quality weld and they may be qualified even at lower than −50 °C temperature environment. Resolving one factor is insufficient to achieve high integrity of welded joints in large weld depths where the stability and the control of the keyhole is limited, as well as the microstructural control. It is important to note that in this work, the weakest part of the welds was tested (i.e., the root area), containing large areas of solidification cracks and brittle bainitic-martensitic microstructures. The upper weld fusion zones would provide higher toughness.

4. Conclusions

According to the experimental observations in double-sided laser-arc hybrid welding of 45 mm thick high strength low alloy steel, the following conclusions are drawn:

- Y-groove beveling provided the ability to achieve full penetration of 45 mm thick plates compared to I-groove beveling at the expense of productivity.
- The density of non-metallic inclusions and their mean diameter decreased rapidly in a linear manner towards the weld root.
- The mean diameter of non-metallic inclusions showed a strong correlation with the cooling time $\Delta t_{8/5}$.
- The standard laser-arc hybrid welding provided predominantly bainitic-martensitic microstructure in the root area with high hardness due to high cooling rate and lack of filler wire.
- Preplaced filler wire in the groove prior welding significantly enhanced the density of non-metallic inclusions; henceforth a higher volume fraction of acicular ferrite was formed.
- Preheating of plates prior welding showed a positive effect on the nucleation and growth of acicular ferrite on non-metallic inclusions by prolonging the cooling time almost by three-fold.
- Higher preheating temperatures than 170 °C provided noticeable softening in the HAZ near the surface showing the limitation of the method.
- The root area of deep welds contained much porosity due to instabilities of the keyhole but within limits.
- Large centerline hot cracks located in root area were formed due to high hardness and high solidification rates. This restricted the characterization of toughness in the HAZ indicating that the weld metal had lower toughness.
- Preheating prior welding was an effective method to reduce porosity in the root area but had low influence in reduction of centerline hot cracks. Therefore, hot cracks supposed to be mainly formed due to high stresses involved during solidification.
- High volume fraction of acicular ferrite nucleation was hindered by insufficiently large mean diameter of non-metallic inclusions (< 200 nm) and unfavorable chemical composition. This opens new possibilities to further enhance weld metal properties by using more adapted filler wires at fast cooling rates providing sufficiently large mean diameter of NMIs and their chemical composition for improved nucleation.
- Significant improvement of impact toughness in the weld metal was achieved (from 11.5 to 46 J) by combining both preplaced filler wire and preheating methods due to higher AF vol%.
- Fracture surface inspection by SEM revealed transition from cleavage to fibrous fracture mode with increase of AF vol%.

Supplementary data to this article can be found online at https://doi.org/10.1016/j.jmapro.2022.08.026.

Declaration of competing interest

The authors declare that they have no known competing financial interests or personal relationship that could have appeared to influence the work in this paper.

Acknowledgements

This publication has been funded by the SFI PhysMet (Centre for Research-based Innovation, 309584). The authors gratefully acknowledge the financial support from the Research Council of Norway and the partners of the SFI PhysMet.

References

[1] Kaplan A. A model of deep penetration laser welding based on calculation of the keyhole profile. J Phys D Appl Phys 1994;27(9):1805–14.
[2] Quintino L, Costa A, Miranda R, Yapp D, Kumar V, Kong CJ. Welding with high power fiber lasers – a preliminary study. Mater Des 2007;28(4):1231–7. https://doi.org/10.1016/j.matdes.2006.01.009.
[3] Sokolov M, Salminen A, Kuznetsov M, Tsibulskiy I. Laser welding and weld hardness analysis of thick section S355 structural steel. Mater Des 2011;32(10):5127–31. https://doi.org/10.1016/j.matdes.2011.05.053.
[4] Shcherbakov EA, Fomin VV, Abramov AA, Ferin AA, Mochalov DV, Gapontsev VP. Industrial grade 100 kW power CW fiber laser. In: Advanced Solid State Lasers. Optical Society of America; 2013. https://doi.org/10.1364/ASSL.2013.ATh4A.2.
[5] Kawahito Y, Wang H, Katayama S, Sumimori D. Ultra high power (100 kW) fiber laser welding of steel. Opt Lett 2018;43(19):4667–70. https://doi.org/10.1364/OL.43.004667.
[6] Katayama S, Yohei A, Mizutani M, Kawahito Y. Development of deep penetration welding technology with high brightness laser under vacuum. Phys. Procedia 2011;12(Part A(0)):75–80. https://doi.org/10.1016/j.phpro.2011.03.010.
[7] Reisgen U, Olschok S, Jakobs S, Turner C. Laser beam welding under vacuum of high grade materials. Weld World 2016;60(3):403–13. https://doi.org/10.1007/s40194-016-0302-3.
[8] Miranda R, Costa A, Quintino L, Yapp D, Iordachescu D. Characterization of fiber laser welds in X100 pipeline steel. Mater Des 2009;30(7):2701–7. https://doi.org/10.1016/j.matdes.2008.09.042.
[9] Bakir N, Üstündağ Ö, Gumenyuk A, Rethmeier M. Experimental and numerical study on the influence of the laser hybrid parameters in partial penetration welding on the solidification cracking in the weld root. Weld World 2020;64(3):501–11. https://doi.org/10.1007/s40194-020-00847-w.
[10] Wiklund G, Akselsen OM, Sørgjerd AJ, Kaplan A. Geometrical aspects of hot cracks in laser-arc hybrid welding. J Laser Appl 2014;26. https://doi.org/10.2351/1.4827135.
[11] Bunaziv I, Frostevarg J, Ren X, Kaplan AFH, Akselsen OM. Porosity and solidification cracking in welded 45 mm thick steel by fiber laser-MAG process. Procedia Manuf 2019;36:101–11. https://doi.org/10.1016/j.promfg.2019.08.015.
[12] Üstündağ Ö, Gook S, Gumenyuk A, Rethmeier M. Hybrid laser arc welding of thick high-strength pipeline steels of grade X120 with adapted heat input. J Mater Process Technol 2020;275:116358. https://doi.org/10.1016/j.jmatprotec.2019.116358.
[13] Bunaziv I, Akselsen OM, Frostevarg J, Kaplan AFH. Deep penetration fiber laser-arc hybrid welding of thick HSLA steel. J Mater Process Technol 2018;256:216–28. https://doi.org/10.1016/j.jmatprotec.2018.02.026.
[14] Bunaziv I, Frostevarg J, Akselsen OM, AFH Kaplan. Process stability during fiber laser-arc hybrid welding of thick steel plates. Opt Lasers Eng 2018;102(Supplement C):34–44. https://doi.org/10.1016/j.optlaseng.2017.10.020.
[15] Li Y, Geng S, Zhu Z, Wang Y, Mi G, Jiang P. Effects of heat source configuration on the welding process and joint formation in ultra-high power laser-MAG hybrid welding. J Manuf Process 2022;77:40–53. https://doi.org/10.1016/j.jmapro.2022.02.045.
[16] Bhadeshia HKDH, Honeycombe RWK. Steels: microstructure and properties. 3rd ed. Butterworth-Heinemann; 2006.
[17] Díaz-Fuentes M, Iza-Mendia A, Gutiérrez I. Analysis of different acicular ferrite microstructures in low-carbon steels by electron backscattered diffraction. Study of their toughness behavior. Metall Mater Trans A 2003;34(11):2505–16. https://doi.org/10.1007/s11661-003-0010-7.
[18] Wan XL, Wang HH, Cheng L, Wu KM. The formation mechanisms of interlocked microstructures in low-carbon high-strength steel weld metals. Mater. Charact 2012;67(Supplement C):41–51. https://doi.org/10.1016/j.matchar.2012.02.007.
[19] Farrar RA, Harrison PL. Acicular ferrite in carbon-manganese weld metals: an overview. J Mater Sci 1987;22(11):3812–20. https://doi.org/10.1007/BF01133327.
[20] Akselsen OM, Grong Ø. Prediction of weld metal Charpy V notch toughness. Mater Sci Eng A 1992;159(2):187–92. https://doi.org/10.1016/0921-5093(92)90288-C.
[21] Loder D, Michelic S, Bernhard C. Acicular ferrite formation and its influencing factors-a review. J. Mater. Sci. Res. 2017;6(1). https://doi.org/10.5539/jmsr.v6n1p24.
[22] Victor B, Nagy B, Ream S, Farson D. High brightness hybrid welding of steel. ICALEO 2009:79–88. https://doi.org/10.2351/1.5061646.
[23] Suder W, Ganguly S, Williams S, Yudodibroto BYB. Penetration and mixing of filler wire in hybrid laser welding. J Mater Process Technol 2021;291:117040. https://doi.org/10.1016/j.jmatprotec.2020.117040.
[24] Karhu M, Kujanpää V, Eskelinen H, Salminen A. Filler metal mixing behaviour of 10 mm thick stainless steel butt-joint welds produced with laser-arc hybrid and laser cold-wire processes. Appl. Sci. 2019;9(8):1685. https://doi.org/10.3390/app9081685.
[25] Meng X, Artinov A, Bachmann M, Rethmeier M. Numerical and experimental investigation of thermo-fluid flow and element transport in electromagnetic stirring enhanced wire feed laser beam welding. Int J Heat Mass Transf 2019;144:118663. https://doi.org/10.1016/j.ijheatmasstransfer.2019.118663.
[26] Meng X, Bachmann M, Artinov A, Rethmeier M. Experimental and numerical assessment of weld pool behavior and final microstructure in wire feed laser beam welding with electromagnetic stirring. J. Manuf. Process 2019;45:408–18. https://doi.org/10.1016/j.jmapro.2019.07.021.
[27] Bunaziv I, Wenner S, Ren X, Frostevarg J, Kaplan AFH, Akselsen OM. Filler metal distribution and processing stability in laser-arc hybrid welding of thick HSLA steel. J Manuf Process 2020;54:228–39. https://doi.org/10.1016/j.jmapro.2020.02.048.
[28] Wahba M, Mizutani M, Katayama S. Single pass hybrid laser-arc welding of 25 mm thick square groove butt joints. Mater. Des. 2016;97(Supplement C):1–6. https://doi.org/10.1016/j.matdes.2016.02.041.
[29] Li L, Mi G, Wang C. A comparison between induction pre-heating and induction post-heating of laser-induction hybrid welding on S690QL steel. J Manuf Process 2019;43:276–91. https://doi.org/10.1016/j.jmapro.2019.05.003.

[30] Turichin G, Kuznetsov M, Pozdnyakov A, Gook S, Gumenyuk A, Rethmeier M. Influence of heat input and preheating on the cooling rate, microstructure and mechanical properties at the hybrid laser-arc welding of API 5L X80 steel. Procedia CIRP 2018;74:748–51. https://doi.org/10.1016/j.procir.2018.08.018.
[31] Babu SS. The mechanism of acicular ferrite in weld deposits. Curr Opin Solid State Mater Sci 2004;8(3):267–78. https://doi.org/10.1016/j.cossms.2004.10.001.
[32] Bunaziv I, Akselsen OM, Frostevarg J, Kaplan AFH. Laser-arc hybrid welding of thick HSLA steel. J Mater Process Technol 2018;259:75–87. https://doi.org/10.1016/j.jmatprotec.2018.04.019.
[33] Zajac S, Schwinn V, Tacke KH. Characterisation and quantification of complex bainitic microstructures in high and ultra-high strength linepipe steels. Mater Sci Forum 2005;500–501:387–94. https://doi.org/10.4028/www.scientific.net/msf.500-501.387.
[34] Ricks RA, Howell PR, Barritte GS. The nature of acicular ferrite in HSLA steel weld metals. J Mater Sci 1982;17(3):732–40. https://doi.org/10.1007/bf00540369.
[35] Yokomizo T, Enomoto M, Umezawa O, Spanos G, Rosenberg RO. Three-dimensional distribution, morphology, and nucleation site of intragranular ferrite formed in association with inclusions. Mater Sci Eng A 2003;344(1):261–7. https://doi.org/10.1016/S0921-5093(02)00411-2.
[36] You Y, Shang C, Wenjin N, Subramanian S. Investigation on the microstructure and toughness of coarse grained heat affected zone in X-100 multi-phase pipeline steel with high Nb content. Mater Sci Eng A 2012;558:692–701. https://doi.org/10.1016/j.msea.2012.08.077.
[37] Cao R, Li J, Liu DS, Ma JY, Chen JH. Micromechanism of decrease of impact toughness in coarse-grain heat-affected zone of HSLA steel with increasing welding heat input. Metall Mater Trans A 2015;46(7):2999–3014. https://doi.org/10.1007/s11661-015-2916-2.
[38] Wang XL, Wang ZQ, Dong LL, Shang CJ, Ma XP, Subramanian SV. New insights into the mechanism of cooling rate on the impact toughness of coarse grained heat affected zone from the aspect of variant selection. Mater. Sci. Eng., A 2017;704 (Supplement C):448–58. https://doi.org/10.1016/j.msea.2017.07.095.
[39] Zhou Y, Jia T, Zhang X, Liu Z, RDK Misra. Microstructure and toughness of the CGHAZ of an offshore platform steel. J. Mater. Process. Technol 2015;219 (Supplement C):314–20. https://doi.org/10.1016/j.jmatprotec.2014.12.017.
[40] Zacharia T. Dynamic stresses in weld metal hot cracking. Weld Res Suppl 1994;73:167–72.
[41] Agarwal G, Kumar A, Richardson IM, Hermans MJM. Evaluation of solidification cracking susceptibility during laser welding in advanced high strength automotive steels. Mater Des 2019;183:108104. https://doi.org/10.1016/j.matdes.2019.108104.
[42] Bakir N, Artinov A, Gumenyuk A, Bachmann M, Rethmeier M. Numerical simulation on the origin of solidification cracking in laser welded thick-walled structures. Metals 2018;8(6):406.
[43] Chen X, Pang S, Shao X, Wang C, Zhang X, Jiang P, Xiao J. Sub-microsecond vapor plume dynamics under different keyhole penetration regimes in deep penetration laser welding. J Phys D Appl Phys 2017;50(20):205601. https://doi.org/10.1088/1361-6463/aa69b7.
[44] Pang S, Shao X, Li W, Chen X, Gong S. Dynamic characteristics and mechanisms of compressible metallic vapor plume behaviors in transient keyhole during deep penetration fiber laser welding. Appl Phys A 2016;122(7):702. https://doi.org/10.1007/s00339-016-0230-5.
[45] Zhang LJ, Zhang JX, Gumenyuk A, Rethmeier M, Na SJ. Numerical simulation of full penetration laser welding of thick steel plate with high power high brightness laser. J Mater Process Technol 2014;214(8):1710–20. https://doi.org/10.1016/j.jmatprotec.2014.03.016.
[46] Volpp J, Vollertsen F. Modeling keyhole oscillations during laser deep penetration welding at different spatial laser intensity distributions. Prod Eng 2015;9(2):167–78. https://doi.org/10.1007/s11740-014-0594-3.
[47] Eriksson I, Powell J, Kaplan AFH. Melt behavior on the keyhole front during high speed laser welding. Opt Lasers Eng 2013;51(6):735–40. https://doi.org/10.1016/j.optlaseng.2013.01.008.
[48] Zhang Z, Farrar RA. Role of non-metallic inclusions in formation of acicular ferrite in low alloy weld metals. Mater Sci Technol 1996;12(3):237–60. https://doi.org/10.1179/mst.1996.12.3.237.
[49] Kluken AO, Grong ØJMTA. Mechanisms of inclusion formation in Al−Ti−Si−Mn deoxidized steel weld metals 1989;20(8):1335–49. https://doi.org/10.1007/bf02665492.
[50] Lee T-K, Kim HJ, Kang BY, Hwang SK. Effect of inclusion size on the nucleation of acicular ferrite in welds. ISIJ Int 2000;40(12):1260–8. https://doi.org/10.2355/isijinternational.40.1260.
[51] Seo K, Kim Y, Evans GM, Lee C, Kim H-J. Formation of Mn-depleted zone in Ti-containing weld metals. Weld World 2015;59:373–80. https://doi.org/10.1007/s40194-014-0207-y.
[52] Tweed JH, Knott JF. Micromechanisms of failure in CMn weld metals. Acta Metall 1987;35(7):1401–14. https://doi.org/10.1016/0001-6160(87)90087-3.
[53] Lan L, Kong X, Qiu C, Zhao D. Influence of microstructural aspects on impact toughness of multi-pass submerged arc welded HSLA steel joints. Mater. Des. 2016;90(Supplement C):488–98. https://doi.org/10.1016/j.matdes.2015.10.158.
[54] van der Eijk C, Grong O, Walmsley J. Mechanisms of inclusion formation in low alloy steels deoxidised with titanium. Mater Sci Technol 2000;16(1):55–64. https://doi.org/10.1179/026708300773002663.
[55] Loder D, Michelic SK. Systematic investigation of acicular ferrite formation on laboratory scale. Mater Sci Technol 2017;33(2):162–71. https://doi.org/10.1080/02670836.2016.1165902.
[56] Evans GM. Microstructure and properties of ferritic steel welds containing Al and Ti. Weld J 1995;74.
[57] Seo K, Kim K-h, Kim HJ, Ryoo H, Evans GM, Lee C. Microstructural and inclusion characteristics of C-Mn steel welds at a minimal level of titanium. Met Mater Int 2020;26(8):1226–34. https://doi.org/10.1007/s12540-019-00390-4.
[58] Fattahi M, Nabhani N, Hosseini M, Arabian N, Rahimi E. Effect of ti-containing inclusions on the nucleation of acicular ferrite and mechanical properties of multipass weld metals. Micron 2013;45:107–14. https://doi.org/10.1016/j.micron.2012.11.004.
[59] Dabiri AR, Yousefi Mojallal R, Ahmadi E, Fattahi M, Amirkhanlou S, Fattahi Y. Effect of ZrO2 nanoparticles on the impact properties of shielded metal arc welds. Mater. Lett. 2015;158(Supplement C):325–8. https://doi.org/10.1016/j.matlet.2015.05.159.
[60] Wang C, Misra RDK, Shi MH, Zhang PY, Wang ZD, Zhu FX, et al. Transformation behavior of a Ti–Zr deoxidized steel: Microstructure and toughness of simulated coarse grain heat affected zone. Mater. Sci. Eng., A 2014;594(Supplement C):218–28. https://doi.org/10.1016/j.msea.2013.11.028.
[61] Thewlis G, Chao WT, Harrison PL, Rose AJ. Acicular ferrite development in autogenous laser welds using cerium sulphide particle dispersed steels. Mater Sci Technol 2008;24(7):771–86. https://doi.org/10.1179/174328408X293621.
[62] Lambert-Perlade A, Sturel T, Gourgues AF, Besson J, Pineau A. Mechanisms and modeling of cleavage fracture in simulated heat-affected zone microstructures of a high-strength low alloy steel. Metall Mater Trans A 2004;35(3):1039–53. https://doi.org/10.1007/s11661-004-0030-y.
[63] Zhou SB, Hu F, Zhou W, Cheng L, Hu CY, Wu KM. Effect of retained austenite on impact toughness and fracture behavior of medium carbon submicron-structured bainitic steel. J Mater Res Technol 2021;14:1021–34. https://doi.org/10.1016/j.jmrt.2021.07.011.
[64] Saini N, Pandey C, Mahapatra MM, Narang HK, Mulik RS, Kumar P. A comparative study of ductile-brittle transition behavior and fractography of P91 and P92 steel. Eng Fail Anal 2017;81:245–53. https://doi.org/10.1016/j.engfailanal.2017.06.044.
[65] Mao G, Cayron C, Cao R, Logé R, Chen J. The relationship between low-temperature toughness and secondary crack in low-carbon bainitic weld metals. Mater Charact 2018;145:516–26. https://doi.org/10.1016/j.matchar.2018.09.012.
[66] Bhadeshia HKDH. Bainite in steels: transformations, microstructure and properties. 2nd ed. IOM Communications; 2001.